

Title: Habitable Worlds Formed at Cosmic Dawn

Authors: Daniel J. Whalen^{1*}, Eduard I. Vorobyov², Muhammad A. Latif^{3*}, Christopher Jessop¹, Ryoki Matsukoba⁴, Takashi Hosokawa⁵, Alexander M. Skliarevskii⁶, Devesh Nandal⁷, Nicholas P. Herrington⁸

Affiliations:

¹Institute of Cosmology and Gravitation, University of Portsmouth; Portsmouth PO1 3FX, UK.

*Corresponding author. Email: dwhalen1999@gmail.com, latifne@gmail.com

²Department of Astrophysics, University of Vienna, Vienna, 1180, Austria.

³Physics Department, College of Science, United Arab Emirates University; PO Box 15551, Al-Ain, UAE.

⁴Department of Physics, Graduate School of Science, Kyoto University, Sakyo, Kyoto 606-8502, Japan.

⁵Department of Physics, Graduate School of Science, Kyoto University, Sakyo, Kyoto 606-8502, Japan.

⁶Research Institute of Physics, Southern Federal University, Rostov-on-Don 344090, Russia.

⁷Department of Astronomy, University of Virginia, Charlottesville, VA 22904, USA.

⁸School of Physics and Astronomy, University of Exeter, Stocker Road, Exeter, EX4 4QL, UK.

Abstract: Primordial supernovae were the first, great nucleosynthetic engines in the Universe, forging the elements required for the later formation of planets and life. Here we show that planetesimals, the precursors of terrestrial planets, formed around low-mass stars in the debris of the first cosmic explosions 200 Myr after the Big Bang, before the first galaxies and far earlier than previously thought. A dense core in one of these explosions collapsed to a protoplanetary disk in which several Earth masses of planetesimals formed 0.46 - 1.66 AU from their parent 0.7 M_{\odot} star, where equilibrium temperatures varied from 269 K to 186 K, in water mass fractions that were only a factor of a few less than in the Solar System today. Habitable worlds thus formed among the first generation of stars in the Universe, before the advent of the first galaxies.

Main Text: The cosmic Dark Ages ended with the birth of primordial (or Pop III) stars in small cosmological halos at redshifts $z \sim 25$, 100 Myr after the Big Bang. It is generally thought that they were a few dozen to a few hundred M_{\odot} (M_{\odot} , solar mass) (1-4). 8 - 30 M_{\odot} Pop III stars died as core-collapse supernovae (CC SNe) and 90 - 260 M_{\odot} Pop III stars died as pair-instability (PI) SNe (5-7). These explosions enriched the early cosmos with the first heavy elements in the Universe (8-12) and the distinctive ‘odd-even’ nucleosynthetic imprint of PI SNe, which can be up to 100 times the energy of a CC SN, has now been found in the fossil abundance record, confirming that these highly energetic transients occurred at early epochs (13, 14).

Ionizing UV flux from the star creates an H II region that is 100 - 5000 pc in radius (15-17). After the star explodes, the SN shock cools as it plows up gas in the relic H II region, first by bremsstrahlung X-ray emission and then by collisional excitation and ionization of H and He (18, 19). Cooling triggers the formation of hydrodynamical instabilities in the shock that mix SN ejecta with gas in the halo, enriching it with dust and heavy elements and, in some cases, creating dense cloud cores (20, 21). We have modeled the formation of such a core in a PI SN at $z \sim 20$ in cosmological environments with the Enzo code and its subsequent collapse to a protoplanetary disk and planetesimals with the FEOSAD code.

Results: In our Enzo simulation a 200 M_{\odot} star forms in a $2.2 \times 10^7 M_{\odot}$ halo at $z = 17.8$. It lives for 2.6 Myr and then explodes with an energy of 2.8×10^{52} erg, ejecting 113 M_{\odot} of metals with 55 M_{\odot} of oxygen. Ionizing UV flux from the star creates an anisotropic H II region with a final radius of about 500 pc. The I-front fails to break out of the halo so the explosion occurs in a trapped H II region with somewhat higher internal densities of $\sim 1 \text{ cm}^{-3}$. The PI SN is shown in Fig. 1, where the relic H II region is visible as the 2000 – 10,000 K gas surrounding the ejecta in the halo.

As shown in the phase diagrams in Fig. S1, the hot PI SN bubble promptly enriches ambient gas to high (and even supersolar) metallicities at early times, as in previous cosmological simulations (22). Hydrodynamical instabilities in the expanding bubble produce turbulent density fluctuations that form a compact clump from gas that is already at a metallicity $Z = 0.04 Z_{\odot}$ (Z_{\odot} , solar metallicity). As shown in Fig. 1, this cloud core becomes self-gravitating and contracts to a radius of ~ 0.01 pc with a mass of 35 M_{\odot} by 3 Myr after the explosion. This structure begins to collapse at much earlier times than in previous chemical enrichment scenarios (9, 23) because it is born at relatively high metallicities that cause it to rapidly cool. As shown in Fig. 2, Jeans masses at the center of the clump fall to $\sim 1 M_{\odot}$ by the end of the simulation, indicating that gas in the center of the core can fragment and collapse on this mass scale.

We show the gravitational collapse of a 1 M_{\odot} fragment of this gas to a protoplanetary system in FEOSAD in Fig. S2. As the clump contracts, it spins up and a disk forms when the inspiralling material reaches the centrifugal barrier in the vicinity of the nascent protostar. The disk quickly grows in size and mass owing to continuing infall of matter from the parent clump and a spiral pattern soon appears. Fig. S3 shows that the Toomre Q-parameter in the disk dips below the threshold value of $\sqrt{3}$ for the gravitational instability (GI) and spiral arms begin to develop.

The GI transports mass radially inward via gravitational torques (24, 25). In this disk, the GI is strongest in its intermediate and outer regions but diminishes in its inner few astronomical units (AU), where gas temperatures and rates of shear are too high for the instability to be sustained.

Fig. S4 shows that the effective α -parameter, which is a measure of the efficiency of mass transport via gravitational torques (25, 26), is smallest in the inner several AU but quickly increases with distance from the star. The radially increasing strength of the GI causes a bottleneck in mass transport that creates a dead zone in the inner several AU where mass transport is heavily reduced. The dead zone is characterized by local gas density and pressure enhancements, as shown in Fig. S5.

As the Stokes numbers of dust grow to ≥ 0.001 in the disk, it decouples from gas and begins to drift inward. However, this inward drifting dust is effectively trapped in the dead zone, leading to a local dust enhancement that in turn promotes grain growth via mutual collisions. Approximately 20 kyr after disk formation, the conditions in the dead zone become favorable to the development of the streaming instability (see Supplementary Data Eqs. 2 and 3), converting mm-sized dust grains into planetesimals, the main building blocks of planets. Fig. 3 shows the global structure of the disk and its inner several AU where the dead zone is localized and the process of dust to planetesimal conversion takes place. A narrow ring of dust is visible at ~ 0.5 AU, while the planetesimals are spread around the dust ring in an annulus with a width of ~ 0.5 AU. The ring of planetesimals is broader because the dust ring slightly migrated in and out while the disk evolved.

Fig. 4 shows the evolution of the stellar, disk, and total planetesimal masses with time. By the end of the simulation the star has reached $0.3 M_{\odot}$ but its final mass is expected to be at least twice as large, given typical mass losses via winds and jets (27). The gas disk mass is about 50 - 60% that of the star. The dust mass in the disk initially reaches $\sim 15 M_{\oplus}$ (M_{\oplus} , Earth masses) owing to mass supply from the parent clump, but then saturates. It levels off because luminosity bursts in the disk evaporate the dust by heating it above the sublimation threshold (see Supplementary Data Eq 1). The bursts are caused by episodic protostellar accretion events like those routinely observed in the Milky Way (28-30) but have also been predicted to occur in primordial star formation (31, 32). The total planetesimal mass levels off at $\sim 5 M_{\oplus}$ soon after the onset of the bursts. While these energetic events limit planetesimal formation in the disk, their total mass is sufficient to form an Earth-type planet via oligarchic growth of colliding planetesimals (33, 34), especially if the growth process of the most massive "oligarchs" is promoted by pebble accretion (35, 36). Indeed, the mass of pebbles in the disk is several Earth masses, as shown in Fig. S6.

Discussion and Conclusion: All known prerequisites for planet formation in this core are fulfilled: dust growth, dust enhancement in a dead zone, onset of the streaming instability, and conversion of dust to planetesimals. These planets could be detected as extinct worlds around ancient, metal-poor stars in the Galaxy in future exoplanet surveys (37). Although the protoplanetary disk in our simulation forms at $z \sim 17$, its host halo could have formed as early as $z \sim 20 - 25$. As noted in the Supplementary Data, we assumed a Lyman-Werner (LW) UV background that enabled the halo to grow to higher masses before forming the $200 M_{\odot}$ star, which presupposes the existence of other Pop III stars in the vicinity, but there are a number of pathways to such halos. Dynamical heating can allow them to reach $1 - 2 \times 10^7 M_{\odot}$ before collapse at just a few J_{21} , the cosmic mean LW background at that era (38), and supersonic baryon streaming motions can create them without UV backgrounds (39, 40) at $z \sim 20 - 25$. Rocky planets could therefore have formed at even earlier times than those here.

We calculated the range of radii over which water could exist in liquid form in the disk with a method considering sub-solar metallicity and assuming that the final stellar mass is 70% that of

the PI SN clump. This range is 0.46 - 1.66 AU and is shown with the green dashed circles in Fig. 3. It encloses the planetesimal formation region, which suggests that planets forming from this debris can harbor water. Our Enzo simulation also shows that water mass fractions in the disk reach mass fractions of $\sim 10^{-4}$, only a factor of a few less than in the Solar System today (41). Habitable worlds thus formed among the first generation of stars even before the advent of the first galaxies, overturning decades of thought on the cosmic origins of life.

References and Notes:

1. S. Hirano, T. Hosokawa, N. Yoshida, K. Omukai, H. W. Yorke, Primordial star formation under the influence of far ultraviolet radiation: 1540 cosmological haloes and the stellar mass distribution. *Mon. Not. Royal Astron. Soc.* 448, 568–587 (2015).
2. K. Sugimura, T. Matsumoto, T. Hosokawa, S. Hirano, K. Omukai, The Birth of a Massive First-star Binary. *Astrophys. J.* 892, L14–L18 (2020).
3. M. A. Latif, D. Whalen, S. Khochfar, The Birth Mass Function of Population III Stars. *Astrophys. J.* 925, 28–32 (2022).
4. R. S. Klessen, S. C. O. Glover, S. C. O., The First Stars: Formation, Properties, and Impact. *Annual Review of Astronomy and Astrophysics* 61, 65–130 (2023).
5. A. Heger, S. E. Woosley, The Nucleosynthetic Signature of Population III. *Astrophys. J.* 567, 532–543 (2002).
6. D. J. Whalen, C. C. Joggerst, C. L. Fryer, M. Stiavelli, A. Heger, D. E. Holz, Finding the First Cosmic Explosions. II. Core-collapse Supernovae. *Astrophys. J.* 768, 95–107 (2013).
7. D. J. Whalen, W. Even, L. H. Frey, J. Smidt, J. L. Johnson, C. C. Lovekin, C. L. Fryer, M. Stiavelli, D. E. Holz, A. Heger, S. E. Woosley, A. L. Hungerford, Finding the First Cosmic Explosions. I. Pair-instability Supernovae. *Astrophys. J.* 777, 110–125 (2013).
8. C. C. Joggerst, A. Almgren, J. Bell, A. Heger, D. J. Whalen, S. E. Woosley, The Nucleosynthetic Imprint of 15-40 Msun Primordial Supernovae on Metal-Poor Stars. *Astrophys. J.* 709, 11–26 (2010).
9. B. D. Smith, J. H. Wise, B. W. O'Shea, M. L. Norman, S. Khochfar, S., The first Population II stars formed in externally enriched mini-haloes. *Mon. Not. Royal Astron. Soc.* 452, 2822–2836 (2015).
10. C. Safranek-Shrader, M. H. Montgomery, M. Milosavljević, V. Bromm, Star formation in the first galaxies - III. Formation, evolution, and characteristics of the first metal-enriched stellar cluster. *Mon. Not. Royal Astron. Soc.* 455, 3288–3302 (2016).
11. M. Magg, T. Nordlander, S. C. O. Glover, C. J. Hansen, M. Ishigaki, A. Heger, R. S. Klessen, C. Kobayashi, A minimum dilution scenario for supernovae and consequences for extremely metal-poor stars. *Mon. Not. Royal Astron. Soc.* 498, 3703–3712 (2020).
12. M. Magg, A. T. P. Schauer, R. S. Klessen, S. C. O. Glover, R. G. Tress, O. Jaura, Metal Mixing in Minihalos: The Descendants of Pair-instability Supernovae. *Astrophys. J.* 929, 119–136 (2022).

13. Q.-F. Xing, G. Zhao, Z.-W. Liu, A. Heger, Z.-W. Han, W. Aoki, Y.-Q. Chen, M. Ishigaki, N. Miho, H.-N. Li, J.-K. Zhao, A metal-poor star with abundances from a pair-instability supernova. *Nature* 618, 712–715 (2023).
14. Y. Yoshii, H. Sameshima, T. Tsujimoto, T., Shigeyama, T. C. Beers, B. A. Peterson, Potential Signature of Population III Pair-instability Supernova Ejecta in the BLR Gas of the Most Distant Quasar at $z = 7.54$. *Astrophys. J.* 937, 61-73 (2022).
15. D. J. Whalen, T. Abel, M. L. Norman, Radiation Hydrodynamic Evolution of Primordial H II Regions. *Astrophys. J.* 610, 14–22 (2004).
16. T. Kitayama, N. Yoshida, H. Susa, M. Umemura, The Structure and Evolution of Early Cosmological H II Regions. *Astrophys. J.* 613, 631–645 (2004).
17. T. Abel, J. H. Wise, G. L. Bryan, The H II Region of a Primordial Star. *Astrophys. J.* 659, L87–L90 (2007).
18. T. Kitayama, N. Yoshida, Supernova Explosions in the Early Universe: Evolution of Radiative Remnants and the Halo Destruction Efficiency. *Astrophys. J.* 630, 675–688 (2005).
19. D. J. Whalen, B. van Veelen, B. W. O'Shea, M. L. Norman, The Destruction of Cosmological Minihalos by Primordial Supernovae. *Astrophys. J.* 682, 49–67 (2008).
20. A. Sluder, J. S. Ritter, C. Safranek-Shrader, M. Milosavljević, V. Bromm, Abundance anomalies in metal-poor stars from Population III supernova ejecta hydrodynamics. *Mon. Not. Royal Astron. Soc.* 456, 1410–1423 (2016).
21. J. S. Ritter, C. Safranek-Shrader, O. Gnat, M. Milosavljević, V. Bromm, V., Confined Population III Enrichment and the Prospects for Prompt Second-generation Star Formation. *Astrophys. J.* 761, 56-70 (2012).
22. M. A. Latif, D. Schleicher, Formation of Population II Star Clusters in the Aftermath of a Pair Instability Supernova. *Astrophys. J.* 902, L31-L40 (2020).
23. G. Chiaki, J. H. Wise, Seeding the second star: enrichment from Population III, dust evolution, and cloud collapse. *Mon. Not. Royal Astron. Soc.* 482, 3933–3949 (2019).
24. E. I. Vorobyov, S. Basu, Secular evolution of viscous and self-gravitating circumstellar discs. *Mon. Not. Royal Astron. Soc.* 393, 822–837 (2009).
25. K. Kratter, G. Lodato, Gravitational Instabilities in Circumstellar Disks. *Ann. Rev. of Astron. Astrophys.* 54, 271–311 (2016).
26. A. Riols, H. Latter, S. J. Paardekooper, Gravitoturbulence and the excitation of small-scale parametric instability in astrophysical discs. *Mon. Not. Royal Astron. Soc.* 471, 317–336 (2017).
27. M. N. Machida, T. Hosokawa, Evolution of protostellar outflow around low-mass proto-star. *Mon. Not. Royal Astron. Soc.* 431, 1719–1744 (2013).
28. M. Audard, *et al.*, Episodic Accretion in Young Stars. In Beuther, H., Klessen, R. S., Dullemond, C. P. & Henning, T. (eds.) *Protostars and Planets VI*, 387–410 (2014).
29. T. Hosokawa *et al.*, Formation of Massive Primordial Stars: Intermittent UV Feedback with Episodic Mass Accretion. *Astrophys. J.* 824, 119 (2016).

30. W. J. Fischer, *et al.* Accretion Variability as a Guide to Stellar Mass Assembly. In Inutsuka, S., Aikawa, Y., Muto, T., Tomida, K. & Tamura, M. (eds.) *Protostars and Planets VII*, vol. 534 of *Astronomical Society of the Pacific Conference Series*, 355 (2023).
31. E. I. Vorobyov, A. L. DeSouza, S. Basu, The Burst Mode of Accretion in Primordial Protostars. *Astrophys. J.* 768, 131 (2013).
32. R. Matsukoba, *et al.*, Disc fragmentation and intermittent accretion on to supermassive stars. *Mon. Not. Royal Astron. Soc.* 500, 4126–4138 (2021).
33. E. Kokubo, S. Ida, Formation of Protoplanets from Planetesimals in the Solar Nebula. *Icarus* 143, 15–27 (2000).
34. J. Chambers, A semi-analytic model for oligarchic growth. *Icarus* 180, 496–513 (2006).
35. M. Lambrechts, A. Johansen, Forming the cores of giant planets from the radial pebble flux in protoplanetary discs. *Astronomy and Astrophysics* 572, A107 (2014).
36. A. Morbidelli, Planet formation by pebble accretion in ringed disks. *Astro. Astrophys.* 638, A1 (2020).
37. C. Boettner, A. Viswanathan, P. Dayal, Exoplanets Across Galactic Stellar Populations with PLATO: Estimating Exoplanet Yields Around FGK Stars for the Thin Disk, Thick Disk and Stellar Halo. arXiv:2407.15917 (2024).
38. J. H. Wise *et al.*, Formation of massive black holes in rapidly growing pre-galactic gas clouds. *Nature* 566, 85–88 (2019).
39. A. Stacy, A., V. Bromm, V., A. Loeb, Effect of Streaming Motion of Baryons Relative to Dark Matter on the Formation of the First Stars. *Astrophys. J.* 730, L1 (2011).
40. A. T. P. Schauer, J. Regan, S. C. O. Glover, R. S. Klessen, The formation of direct collapse black holes under the influence of streaming velocities. *Mon. Not. Royal Astron. Soc.* 471, 4878–4884 (2017).
41. D. J. Whalen, M. A. Latif, C. J. Jessop, Water Formed at Cosmic Dawn, *Nat. Astron.*, accepted.
42. J. P. Ostriker, C. F. McKee, Astrophysical blastwaves. *Reviews of Modern Physics* 60, 1–68 (1988).
43. G. L. Bryan, M. L. Norman, B. W. O'Shea, T. Abel, J. H. Wise, M. J. Turk, D. R. Reynolds, D. C. Collins, P. Wang, S. W. Skillman, B. Smith, R. P. Harkness, J. Bordner, J.-h. Kim, M. Kuhlen, H. Xu, N. Goldbaum, C. Hummels, A. G. Kritsuk, E. Tasker, S. Skory, C. M. Simpson, O. Hahn, J. S. Oishi, G. C. So, F. Zhao, R. Cen, L. Yuan, ENZO: An Adaptive Mesh Refinement Code for Astrophysics. *Astrophys. J. Suppl.* 211, (2014).
44. G. Efstathiou, M. Davis, S. D. M White, C. S. Frenk, Numerical Techniques for Large Cosmological N-body Simulations. *Astrophys. J. Suppl.* 57, 241–260 (1985).
45. H. M. P. Couchman, Mesh-refined P³M: A Fast Adaptive N-Body Algorithm. *Astrophys. J.* 368, L23-L26 (1991).
46. P. Woodward, P. Colella, The Numerical Stimulation of Two-Dimensional Fluid Flow with Strong Shocks. *Journal of Computational Physics* 54, 115–173 (1984).
47. G. L. Bryan, M. L., Norman, J. M. Stone, R. Cen, J. P. Ostriker, A piecewise parabolic method for cosmological hydrodynamics. *Computer Physics Communications* 89, 149–168 (1995).

48. E. F. Toro, M. Spruce, W. Speares, Restoration of the contact surface in the HLL-Riemann solver. *Shock Waves* 4, 25–34 (1994).
49. J. H. Wise, T. Abel, ENZO+MORAY: radiation hydrodynamics adaptive mesh refinement simulations with adaptive ray tracing. *Mon. Not. Royal Astron. Soc.* 414, 3458–3491 (2011).
50. B. D. Smith, G. L. Bryan, S. C. O. Glover, N. J. Goldbaum, M. J. Turk, J. Regan, J. H. Wise, H.-Y. Schive, T. Abel, A. Emerick, B. W. O'Shea, P. Anninos, C. B. Hummels, S. Khochfar, GRACKLE: a chemistry and cooling library for astrophysics. *Mon. Not. Royal Astron. Soc.* 466, 2217–2234 (2017).
51. G. Chiaki, H. Susa, S. Hirano, Metal-poor star formation triggered by the feedback effects from Pop III stars. *Mon. Not. Royal Astron. Soc.* 475, 4378–4395 (2018).
52. F. Santoro, J. M. Shull, Critical Metallicity and Fine-Structure Emission of Primordial Gas Enriched by the First Stars. *Astrophys. J.* 643, 26–37 (2006).
53. D. A. Neufeld, M. J. and Kaufman, Radiative Cooling of Warm Molecular Gas. *Astrophys. J.* 418, 263–273 (1993).
54. D. A. Neufeld, S. Lepp, G. J. Melnick, Thermal Balance in Dense Molecular Clouds: Radiative Cooling Rates and Emission-Line Luminosities. *Astrophys. J. Suppl.* 100, 132–148 (1995).
55. K. Omukai, T. Hosokawa, N. Yoshida, Low-metallicity Star Formation: Prestellar Collapse and Protostellar Accretion in the Spherical Symmetry. *Astrophys. J.* 722, 1793–1815 (2010).
56. O. Hahn, T. Abel, Multi-scale initial conditions for cosmological simulations. *Mon. Not. Royal Astron. Soc.* 415, 2101–2121 (2011).
57. Planck Collaboration, Planck 2015 results. XIII. Cosmological parameters. *Astronomy and Astrophysics* 594, A13–A76 (2016).
58. E. I. Vorobyov, V. Akimkin, O. Stoyanovskaya, Y. Pavlyuchenkov, H. B. Liu, Early evolution of viscous and self-gravitating circumstellar disks with a dust component. *Astro. Astrophys.* 614, A98 (2018).
59. E. I. Vorobyov, *et al.*, Formation of pebbles in (gravito-)viscous protoplanetary disks with various turbulent strengths. *Astro. Astrophys.* 670, A81 (2023).
60. E. I. Vorobyov, S. Basu, The Burst Mode of Accretion and Disk Fragmentation in the Early Embedded Stages of Star Formation. *Astrophys. J.* 719, 1896–1911 (2010).
61. J. M. Stone, M. L. Norman, ZEUS-2D: A Radiation Magnetohydrodynamics Code for Astrophysical Flows in Two Space Dimensions. I. The Hydrodynamic Algorithms and Tests. *Astrophys. J. Suppl.* 80, 753 (1992).
62. E. I. Vorobyov *et al.*, Evolution of dust in protoplanetary disks of eruptive stars. *Astro. Astrophys.* 658, A191 (2022).
63. P. Colella, P. R. Woodward, The Piecewise Parabolic Method (PPM) for Gas-Dynamical Simulations. *Journal of Computational Physics* 54, 174–201 (1984).
64. J. Binney, S. Tremaine, J. Ostriker, *Galactic Dynamics*. Princeton series in astrophysics (Princeton University Press, 1987).
65. E. I. Vorobyov, A. M. Skliarevskii, M. Guedel, T. Molyarova, Primordial dust rings, hidden dust mass, and the first generation of planetesimals in gravitationally unstable protoplanetary disks. arXiv:2404.16151 (2024).

66. N. I. Shakura, R. A. Sunyaev, Black holes in binary systems. Observational appearance. *Astro. Astrophys.* **24**, 337–355 (1973).
67. E. I. Vorobyov, R. Matsukoba, K. Omukai, M. Guedel, Thermal evolution of protoplanetary disks: from β -cooling to decoupled gas and dust temperatures. *Astro. Astrophys.* **638**, A102 (2020).
68. C. B. Henderson, Drag coefficient of spheres in continuum and rarefied flows. *AIAA Journal* **14**, 707–707 (1976).
69. O. P. Stoyanovskaya, F. A. Okladnikov, E. I. Vorobyov, Y. N. Pavlyuchenkov, V. V. Akimkin, Simulations of Dynamical Gas-Dust Circumstellar Disks: Going Beyond the Epstein Regime. *Astronomy Reports* **64**, 107–125 (2020).
70. O. P. Stoyanovskaya, E. I. Vorobyov, V. N. Snytnikov, Analysis of Numerical Algorithms for Computing Rapid Momentum Transfers between the Gas and Dust in Simulations of Circumstellar Disks. *Astronomy Reports* **62**, 455–468 (2018).
71. T. Birnstiel, H. Klahr, B. A. Ercolano, A simple model for the evolution of the dust population in protoplanetary disks. *Astro. Astrophys.* **539**, A148 (2012).
72. J. Blum, G. Wurm, G. The growth mechanisms of macroscopic bodies in protoplanetary disks. *Ann. Rev. of Astron. Astrophys.* **46**, 21–56 (2008).
73. B. Gundlach, J. Blum, The Stickiness of Micrometer-sized Water-ice Particles. *Astrophys. J.* **798**, **34** (2015).
74. C. Pillich, T. Bogdan, J. Landers, G. Wurm, H. Wende, Drifting inwards in protoplanetary discs. II. The effect of water on sticking properties at increasing temperatures. *Astro. Astrophys.* **652**, A106 (2021).
75. H. W. Yorke, P. Bodenheimer, Theoretical Developments in Understanding Massive Star Formation. In Beuther, H., Linz, H. & Henning, T. (eds.) *Massive Star Formation: Observations Confront Theory*, vol. 387 of *Astronomical Society of the Pacific Conference Series*, 189 (2008).
76. T. Hosokawa, K. Omukai, Low-Metallicity Protostars and the Maximum Stellar Mass Resulting from Radiative Feedback: Spherically Symmetric Calculations. *Astrophys. J.* **703**, 1810–1818 (2009).
77. P. Woitke *et al.*, Equilibrium chemistry down to 100 K. Impact of silicates and phyllosilicates on the carbon to oxygen ratio. *Astro. Astrophys.* **614**, A1 (2018).
78. A. N. Youdin, J. Goodman, Streaming Instabilities in Protoplanetary Disks. *Astrophys. J.* **620**, 459–469 (2005).
79. C. C. Yang, A. Johansen, D. Carrera, Concentrating small particles in protoplanetary disks through the streaming instability. *Astro. Astrophys.* **606**, A80 (2017).
80. E. I. Vorobyov, Effect of the initial density and angular-velocity profiles of pre-stellar cores on the properties of young stellar objects. *Astronomy Reports* **56**, 179–192 (2012).
81. K. Omukai, T. Tsuribe, R. Schneider, R., A. Ferrara, Thermal and Fragmentation Properties of Star-forming Clouds in Low-Metallicity Environments. *Astrophys. J.* **626**, 627–643 (2005).
82. E. I. Vorobyov, Lifetime of the Embedded Phase of Low-Mass Star Formation and the Envelope Depletion Rates. *Astrophys. J.* **713**, 1059–1072 (2010).
83. V. L. Polyachenko, E. V. Polyachenko, A. V. Strel’Nikov, Stability criteria for gaseous self-gravitating disks. *Astronomy Letters* **23**, 483–491 (1997).
84. A. Riols, H. Latter, Magnetorotational instability and dynamo action in gravito-turbulent astrophysical discs. *Mon. Not. Royal Astron. Soc.* **474**, 2212–2232 (2018).
85. E. I. Vorobyov, The applicability of the viscous α -parameterization of gravitational instability in circumstellar disks. *New Astron* **15**, 24–38 (2010).

86. J. Schober *et al.*, The Small-scale Dynamo and Non-ideal Magnetohydrodynamics in Primordial Star Formation. *Astrophys. J.* **754**, 99 (2012).
87. M. A. Latif, D. R. G. Schleicher, Magnetic fields in primordial accretion disks. *Astro. Astrophys.* **585**, A151 (2016).
88. P. Sharda, C. Federrath, M. R. Krumholz, The importance of magnetic fields for the initial mass function of the first stars. *Mon. Not. Royal Astron. Soc.* **497**, 336–351 (2020).
89. O. Gressel, N. J. Turner, R. P. Nelson, C. P. McNally, Global Simulations of Protoplanetary Disks With Ohmic Resistivity and Ambipolar Diffusion. *Astrophys. J.* **801**, 84 (2015).
90. K. Kadam, E. I. Vorobyov, A. Kospal, Eruptive Behavior of Magnetically Layered Protoplanetary Disks in Low-metallicity Environments. *Astrophys. J.* **909**, 31 (2021).
91. E. I. Vorobyov, A. M. Skliarevskii, M. Guedel, T. Molyarova, Primordial dust rings, hidden dust mass, and the first generation of planetesimals in gravitationally unstable protoplanetary disks. *Astro. Astrophys.* **687**, A192 (2024).
92. C. F. Gammie, Layered Accretion in T Tauri Disks. *Astrophys. J.* **457**, 355 (1996).
93. W. Xu, P. J. Armitage, Revisiting Collisional Dust Growth in Class 0/I Protostellar Disks: Sweep-up Can Convert a Few $10 M_{\oplus}$ of Dust into Kilogram Pebbles in 0.1 Myr. *Astrophys. J.* **946**, 94 (2023).
94. S. J. Weidenschilling, Aerodynamics of solid bodies in the solar nebula. *Mon. Not. Royal Astron. Soc.* **180**, 57–70 (1977).
95. R. Li, A. N. Youdin, Thresholds for Particle Clumping by the Streaming Instability. *Astrophys. J.* **919**, 107 (2021).
96. K. R. Bell, D. N. C. Lin, Using FU Orionis Outbursts to Constrain Self-regulated Protostellar Disk Models. *Astrophys. J.* **427**, 987 (1994).
97. Z. Zhu, L. Hartmann, C. Gammie, J. C. McKinney, Two-dimensional Simulations of FU Orionis Disk Outbursts. *Astrophys. J.* **701**, 620–634 (2009).
98. I. Bonnell, P. A. Bastien, Binary Origin for FU Orionis Stars. *Astrophys. J.* **401**, L31 (1992).
99. R. Dong *et al.*, A likely flyby of binary protostar Z CMa caught in action. *Nat. Astron.* **6**, 331–338 (2022).
100. S. Nayakshin, G. Lodato, FU Ori outbursts and the planet-disc mass exchange. *Mon. Not. Royal Astron. Soc.* **426**, 70–90 (2012).
101. Topchieva, A., Molyarova, T., Akimkin, V., Maksimova, L. & Vorobyov, E. Ices on pebbles in protoplanetary discs. *Mon. Not. Royal Astron. Soc.* (2024).
102. K. Metzler, D. C. Hezel, J. Nellesen, Various Size-sorting Processes for Millimeter-sized Particles in the Sun’s Protoplanetary Disk? Evidence from Chondrules in Ordinary Chondrites. *Astrophys. J.* **887**, 230 (2019).
103. J. F. Kasting, D. P. Whitmire, R. T. Reynolds, Habitable Zones around Main Sequence Stars. *Icarus* **101**, 108–128 (1993).
104. S. Krijt *et al.*, Chemical Habitability: Supply and Retention of Life’s Essential Elements During Planet Formation. In Inutsuka, S., Aikawa, Y., Muto, T., Tomida, K. & Tamura, M. (eds.) *Protostars and Planets VII*, vol. 534 of *Astronomical Society of the Pacific Conference Series*, **1031** (2023).
105. G. Valle, M. Dell’Omodarme, P. G. Prada Moroni, S. Degl’Innocenti, Evolution of the habitable zone of low-mass stars. Detailed stellar models and analytical relationships for different masses and chemical compositions. *Astro. Astrophys.* **567**, A133 (2014).
106. M. N. Machida, T. Hosokawa, Evolution of protostellar outflow around low-mass protostar. *Mon. Not. Royal Astron. Soc.* **431**, 1719–1744 (2013).
107. de Pater, I. & Lissauer, J. J. *Planetary Sciences* (2001).

108. F. Selsis, *et al.*, Habitable planets around the star Gliese 581? *Astro. Astrophys.* **476**, 1373 – 1387 (2007).
109. R. K. Kopparapu *et al.*, Habitable Zones around Main-sequence Stars: New Estimates. *Astrophys. J.* **765**, 131 (2013).
110. R. M. Ramirez, L. A. Kaltenegger, Volcanic Hydrogen Habitable Zone. *Astrophys. J.* **837**, L4 (2017).

Acknowledgments:

Funding

FWF Grant 14311-N27 (EIV)

United Arab Emirates University UPAR Grant 31S390 (MAL)

United Arab Emirates University UPAR Grant 12S111 (MAL)

STFC Grant ST/505651/1 (CJ)

STFC Grant ST/506345/1 (CJ)

Japan Grants-in-Aid for Scientific Research TH:19H01934, 19KK0353, 21H00041, 22H00149 (RM, TH)

Ministry of Science and Education of the Russian Federation Grant GZ0110/23-10-IF (AMS)

ERC Grant 833925 (Project STAREX) (DN)

VITA Fellowship (DN)

ERC Grant 818940 (Project ICYBOB) (NPH)

Author contributions

Conceptualization: DJW, EIV, MAL

Methodology: DJW, MAL, CJ, EIV

Investigation: DJW, EIV, MAL, CJ, RM, TH

Visualization: MAL, EIV, AMS

Supervision: DJW, MAL, EIV

Writing – original draft: DJW

Writing – review & editing: DJW

Competing interests

Authors declare that they have no competing interests.

Data and materials availability

The code used to produce our cosmological simulations, Enzo 2.6, can be found at <https://bitbucket.org/enzo/enzo-dev/tree/enzo-2.6.1>. The Enzo parameter files and initial conditions files generated by MUSIC that are required to perform the simulations are available at <https://doi.org/10.5281/zenodo.5853118> (DOI: 10.5281/zenodo.5853118). The FEOSAD code and its simulation data can be obtained upon reasonable request. The habitable zone online calculator is accessible at <http://astro.df.unipi.it/stellar-models/HZ/>.

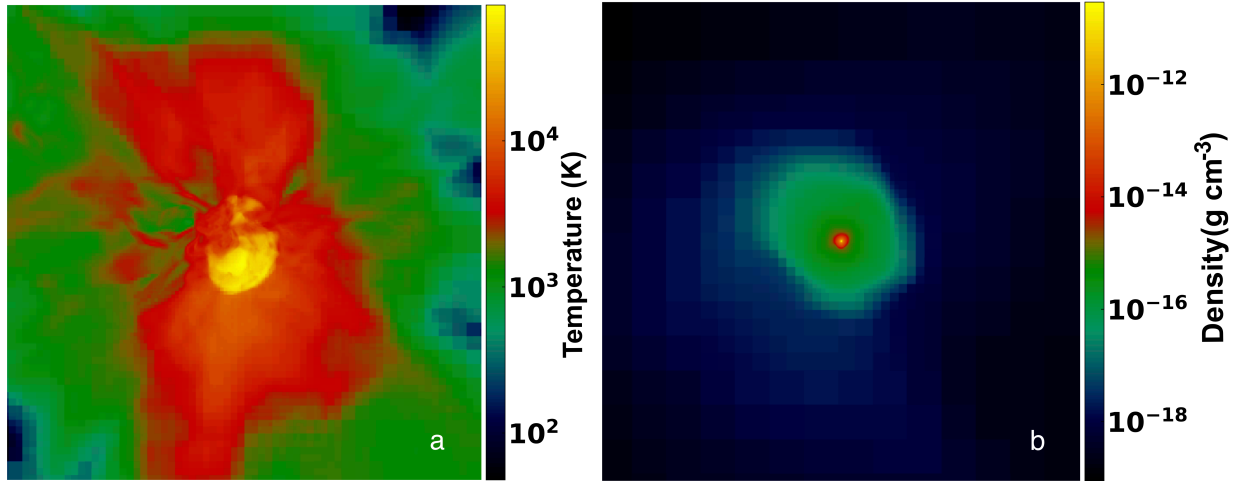


Fig. 1. Explosion of the star and formation of the dense core. The PI SN is shown 0.7 Myr after the explosion in the 1 kpc image in (a). The relic H II region of the star is visible as the 2000 - 10000 K gas surrounding the ejecta. The SN shock reaches temperatures of a few 10^6 K, consistent with analytical approximations (42), but they are limited to 10^5 K in (a) because they are averaged along the line of sight in the cube. The dense core is shown 3.0 Myr after the explosion in the 0.1 pc image in (b), when it has reached a mass of $35 M_{\odot}$ and collapsed to central densities of $6.0 \times 10^{14} \text{ cm}^{-3}$.

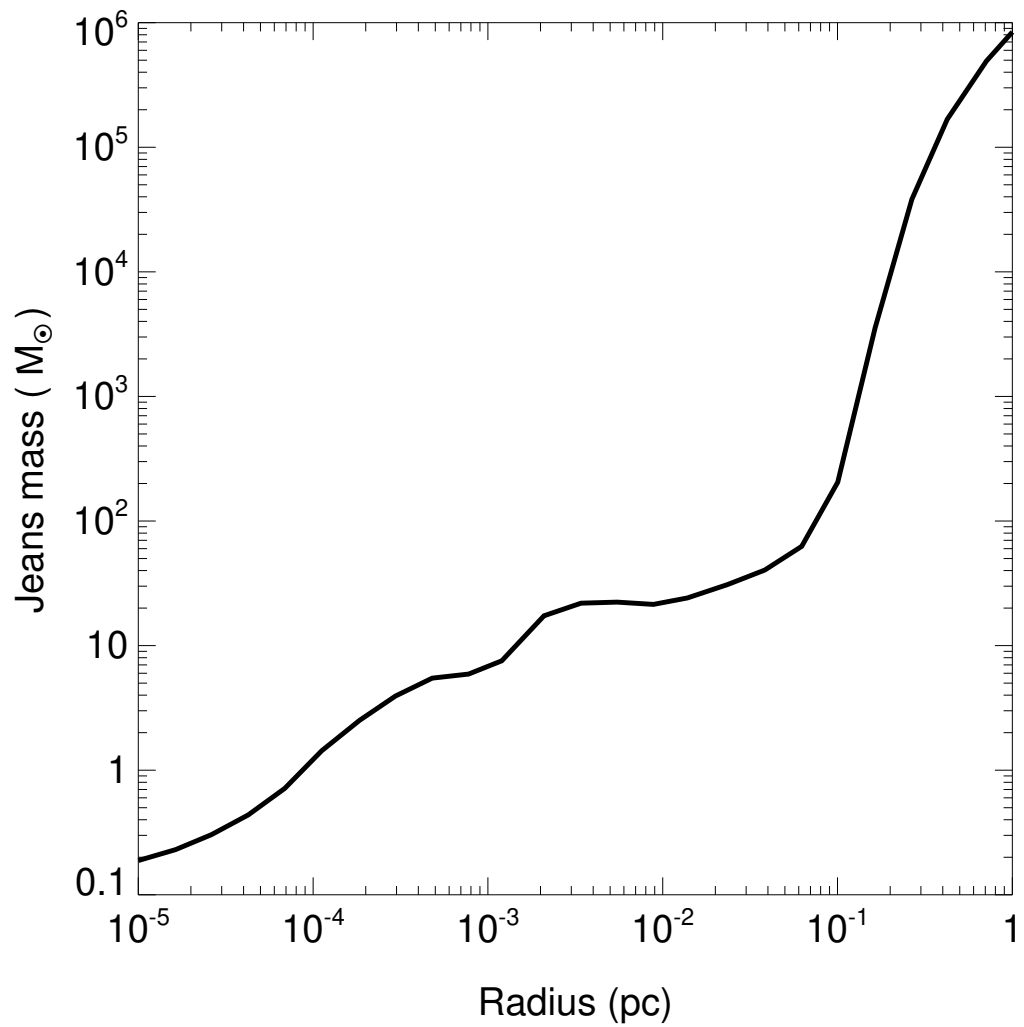


Fig. 2. Jeans masses in the dense core. Gas at the center of the core can fragment on mass scales of $\sim 1 M_{\odot}$.

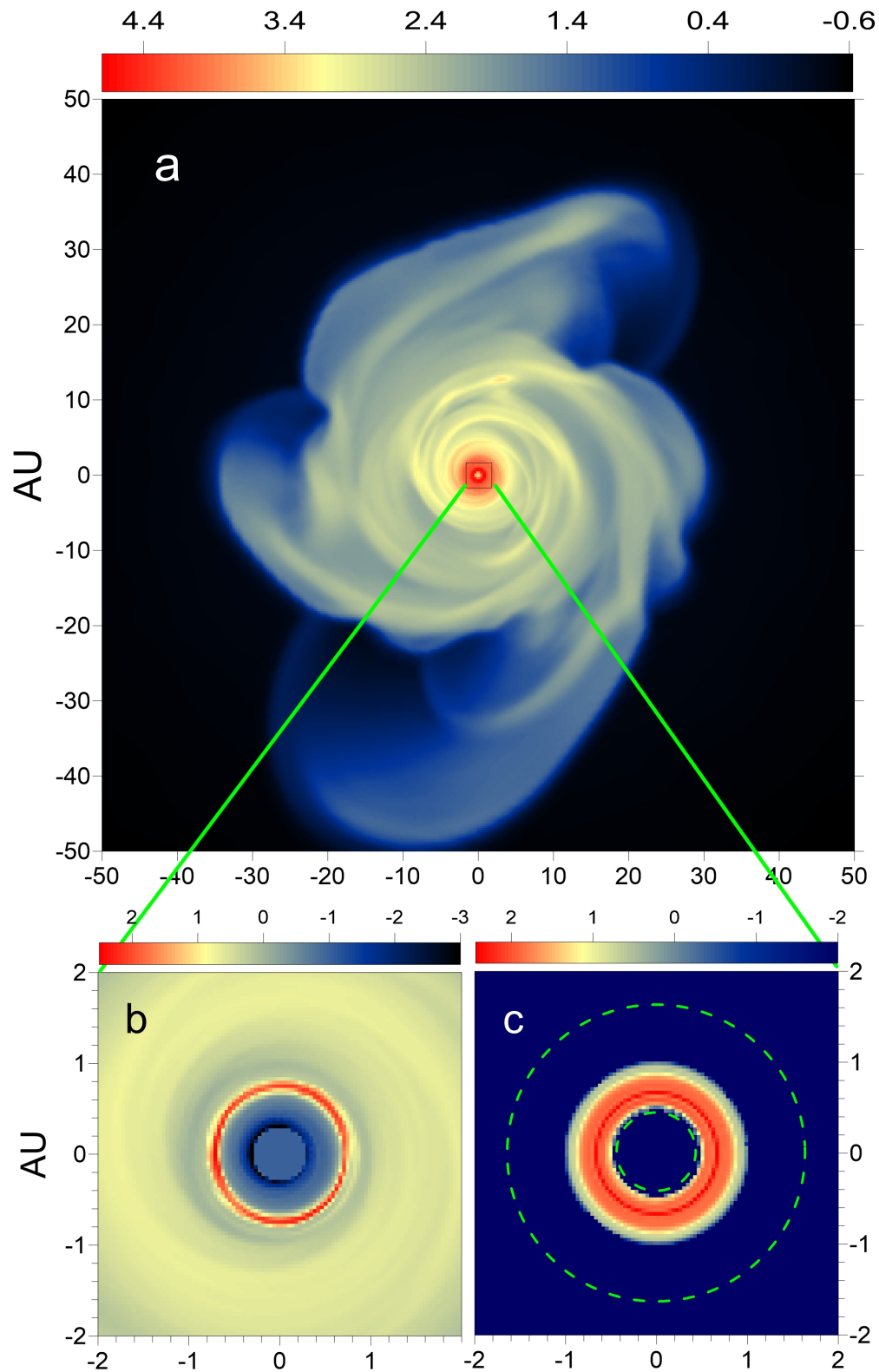


Fig. 3. The protoplanetary disk. Gas, dust and planetesimal distributions are shown 39 kyr after the formation of the protostar in (a) – (c), respectively, where b and c show the central 4 AU of the disk. The green dashed circles indicate where water can exist in liquid form. The color bars are in units of $\log g \text{ cm}^{-2}$.

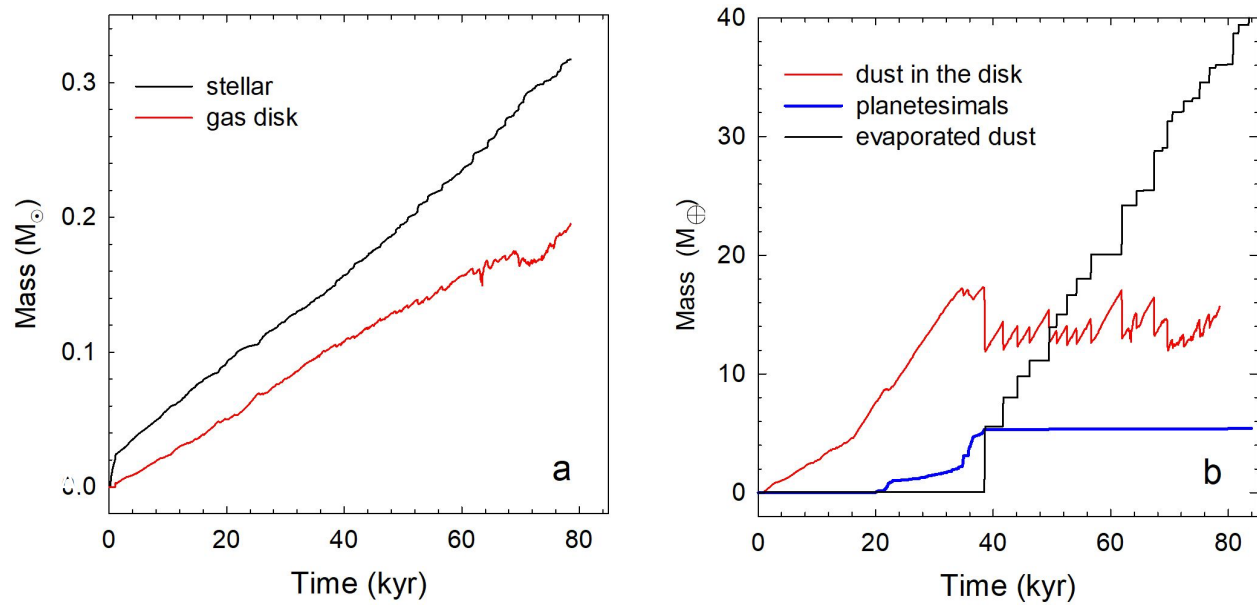


Fig. 4. Evolution of the disk. Star and disk gas masses are shown in (a) from the birth of the protostar. Dust, planetesimal, and evaporated dust masses are shown in (b).

Submitted Manuscript: Confidential

Template revised November 2023

Science



Supplementary Materials for

Habitable Worlds Formed at Cosmic Dawn

Daniel J. Whalen^{1*}, Eduard I. Vorobyov², Muhammad A. Latif^{3*}, Christopher Jessop¹, Ryoki Matsukoba⁴, Takashi Hosokawa⁵, Alexander Skliarevskii⁶, Devesh Nandal⁷, Nicholas P. Herrington⁸

Corresponding author: *dwhalen1999@gmail.com*

The PDF file includes:

Supplementary Text

Figs. S1 to S11

References: 43-110

Supplementary Text

The Enzo (43) adaptive mesh refinement (AMR) code uses an N-body particle-mesh scheme (44, 45) and the piecewise parabolic method (46, 47) to evolve dark matter (DM) and hydrodynamics in cosmological simulations. They are self-consistently coupled to radiation transport, nonequilibrium gas chemistry, and a multigrid Poisson solver for self-gravity. Our simulation employs the HLLC scheme for enhanced stability with strong shocks and rarefaction waves (48). UV photon transport is done with the MORAY raytracing radiation code (49) with four energy bins: H and He ionizing photons, H⁻ photodetachment photons and Lyman-Werner (LW) photons.

We evolve nonequilibrium chemistry with Grackle (50), with 49 reactions in 15 primordial gas species (e⁻, H, H⁺, H₂, H⁻, H₂⁺, HeH⁺, He, He⁺, He²⁺, D, D⁺, D⁻, HD, HD⁺, HeH⁺, D⁻ and HD⁺) and 40 reactions in 17 metal and molecular species (C⁺, C, CH, CH₂, CO⁺, CO, CO₂, O⁺, O, OH⁺, OH, H₂O⁺, H₂O, H₃O⁺, O₂⁺, O₂, Si, SiO, and SiO₂) (51, 23). This fully implicit network includes updates to the gas energy due to heat from H₂ formation as well as collisional excitation and ionization cooling by H and He, recombination cooling, bremsstrahlung cooling, and inverse Compton cooling by the cosmic microwave background (CMB) for $T > 8000$ K. It also does H₂ and HD line cooling for $T < 10,000$ K. We calculate H₂ emission rates for line transitions in 20 rotational and three vibrational levels and HD rates for transitions in three vibrational states. Cooling due to fine structure emission by C⁺, C and O (52) and transitions between rotational levels in OH, H₂O and CO are also included, where the line rates are obtained from interpolations in precomputed tables (53-55). At high densities the gas can become opaque to its own line emission, which reduces cooling rates if photons become trapped. We include corrections to optically thin gas cooling by metal and molecule lines at high densities (23).

We initialized our PI SN simulation in a $1.5 h^{-1}$ Mpc box at $z = 200$ with cosmological initial conditions generated with MUSIC (56) from the second-year Planck best fit lowP + lensing + BAO + JLA + H0 cosmological parameters: $\Omega_M = 0.3089$, $\Omega_\Lambda = 0.691$, $\Omega_b = 0.0486$, $\sigma_8 = 0.816$, $h^{-1} = 0.677$, and $n = 0.967$ (57). We first performed a low-resolution 256^3 unigrid DM-only run to obtain the host halo of the star. We then centered three nested grids on the halo that spanned 10% of the top grid and evolved the halo with full baryonic physics with up to 28 levels of refinement and 16 zones per Jeans length to achieve a maximum resolution of 2.1 AU. We included a LW UV background of $100 J_{21}$, where $J_{21} = 10^{-21}$ erg s⁻¹ Hz⁻¹ steradian⁻¹, out of convenience to delay star formation in the halo until it grew to over $10^7 M_\odot$.

FEOSAD

Following the gravitational contraction of the clump to the protostellar stage in Enzo is prohibitively expensive so we modeled it with the FEOSAD protoplanetary disk code (58, 59). FEOSAD solves the continuity, momentum and energy equations of hydrodynamics for the gas and dust disk subsystems in the thin-disk limit, in which motion is restricted to the disk midplane and vertically integrated disk hydrodynamic quantities are evolved (31, 60). The equations are integrated with the method of finite volumes (61) with dust treated as a pressureless fluid (62), and gas and dust are advected with third-order-accurate piecewise-parabolic interpolation (63). The gravitational potential of the gas-dust disk was evolved with the convolution method (64), which

has been thoroughly tested (65). Turbulent viscosity is modeled with the usual α -parameter approach (66) with $\alpha = 10^{-4}$ everywhere in the disk.

Cooling due to continuum emission by gas and dust, molecular line emission by H₂ and HD, fine-structure line emission by O I (63 μm) and C II (158 μm), and cooling and heating by H ionization and recombination and H₂ dissociation and formation were included in our simulations (67). We evolved a time-dependent non-equilibrium chemical network with 27 reactions to determine mass fractions for the eight species (H, H₂, H⁺, H⁻, D, HD, D⁺, and e⁻) that govern primordial heating and cooling and contribute to molecular line emission. Dust temperatures are calculated from the energy balance on dust grains due to thermal emission, absorption, and collisions with gas. Our method permits decoupling of the gas and dust temperatures in the low density and metallicity regimes, and heating by turbulent viscosity and stellar irradiation are also considered. Gas and dust are dynamically coupled not only by gravity but also by friction, which is calculated with the Henderson friction coefficient (68) as applied in astrophysical contexts (69). This approach allows us to treat drag forces while avoiding discontinuities in the Epstein and Stokes regimes. Gas and dust velocity updates due to mutual friction (including backreaction of dust on gas) are performed with a fully implicit solution procedure that was extensively tested (70).

FEOSAD accounts for dust growth in the framework of the monodisperse dust growth model (59, 71). All dust initially is in the form of sub- μm dust monomers, but they grow in mass and size via mutual collisions and coagulation. The dust growth is limited by the fragmentation barrier, defined as the maximum size of dust grains, a_{frag} , that can be attained via mutual collisions of dust particles, and by the drift barrier, which is treated self-consistently when solving the dynamical equations for the dust component. The fragmentation velocity is set equal to 5.0 m s⁻¹. Laboratory experiments provide a range of values from ~ 1.0 m s⁻¹ for bare silicates to ≥ 10 m s⁻¹ for icy grains (72, 73). However, recent data suggest that silicates may be stickier than usual at higher temperatures. In particular, the fragmentation velocity may increase manyfold above 1000 K (74). Since the main focus of our study is on the inner several AU where temperatures approach this regime (Fig. S5), we have chosen $v_{\text{frag}} = 5.0$ m s⁻¹. Effects caused by variations in v_{frag} are discussed later.

To ease time step limitations imposed by the Courant condition, a sink cell with a radius of 0.3 AU was excised from the center of the grid. Matter passing into the sink is assumed to land on the protostar, which gains mass accordingly. The photospheric luminosity of the protostar is determined with precomputed stellar evolution tracks from the STELLAR code at the given metallicity (75, 76). Photospheric and accretion luminosities affect the thermal balance of the disk via stellar irradiation.

Dust temperatures in the innermost regions of the disk can exceed the threshold for evaporation. To account for this effect, we reduced the dust density exponentially in regions where it is sublimated. The threshold temperature is defined as

$$T_{\text{d,sub}} = 1900 \rho_{\text{g}}^{0.0195} (K),$$

where ρ_{g} is the volume density (in g cm⁻³) obtained from the corresponding gas surface density and the gas disk scale height, H_{g} , under the assumption of local hydrostatic equilibrium. With this

definition of $T_{d,\text{sub}}$, most dust evaporates above 1200 K, in agreement with the ggChem model of dust sublimation and condensation (77). Once evaporated, the dust is removed from the system without being reconstituted at later times.

Dust is converted to planetesimals assuming that the streaming instability is the primary mechanism for planetesimal formation in protoplanetary disks (78). FEOSAD has limitations (resolution, vertically integrated disk characteristics) which makes it difficult to directly model the development of the streaming instability. Therefore, we use criteria derived from numerical studies of the growth of the streaming instability (79):

$$\begin{aligned}\log \xi_{d2g} &\geq 0.10 (\log St)^2 + 0.20 (\log St) - 1.76 \quad (St < 0.1) \\ \log \xi_{d2g} &\geq 0.30 (\log St)^2 + 0.59 (\log St) - 1.57 \quad (St > 0.1)\end{aligned}$$

where $\xi_{d2g} = \Sigma_d / \Sigma_g$ is the dust-to-gas mass ratio and St is the Stokes number. These conditions are complemented by the requirement that the volume density of dust in the disk midplane, ρ_d , be equal to or greater than that of gas, $\zeta = \rho_d / \rho_g \geq 1.0$ (78). The value of ρ_d is obtained from the surface density of dust Σ_d via the dust disk scale height, which scales with turbulent α and St as $H_d = H_g \sqrt{(\alpha / (St + \alpha))}$.

Initial conditions for FEOSAD

We approximate the complex 3D density and velocity distributions of the inner $1 M_\odot$ of the PI SN core by surface density and angular velocity profiles that are inversely proportional to radius. The particular form of the initial density and angular momentum profiles of the contracting prestellar core has minor effect on the properties of the protostellar disk for a given mass (80). The initial dust-to-gas ratio, which defines the total dust mass budget of the contracting prestellar core in FEOSAD, was obtained by averaging the dust and gas content in the PI SN core, resulting in $\xi_{d2g}^{\text{init}} = 4 \times 10^{-4}$. The initial size distribution of dust grains varies from 0.005 - 1.0 μm . Initial species mass fractions and gas and dust temperatures were obtained from a one-zone model of prestellar clouds for the metallicity of the PI SN core (81).

Protoplanetary disk formation and evolution

We show the formation and evolution of the protoplanetary disk in Fig. S2. The protostar forms 24 kyr after the onset of collapse and the disk forms ~ 1.0 kyr later when spinning up and inspiralling material in the clump reaches the centrifugal barrier near the protostar. In this early stage of evolution, infall rates exceed accretion rates onto the protostar (82) so the disk grows in mass and radius. By just 21 kyr after protostar formation, the disk develops a compact but notable spiral structure, which is a signature of the development of the GI. As the disk size increases, the spiral pattern becomes more pronounced.

The susceptibility of the disk to the GI is shown by the radial distribution of the Toomre Q -parameter at $t = 30$ kyr and 40 kyr in Fig. S2, which takes dust into account (58) by

$$Q = \frac{\tilde{c}_s \Omega}{\pi G (\Sigma_g + \Sigma_d)},$$

where $\tilde{c}_s = c_s \sqrt{1 + \xi_{d2g}}$ is the modified sound speed, Σ_g and Σ_d are the surface densities of gas and dust, Ω is the angular velocity of gas, and G the gravitational constant. Since azimuthal averaging of the Q -parameter may be misleading, the Q -values in each cell along the azimuth (at a given distance r) are plotted. Regions of the disk from 1.0 AU to a few tens of AU are prone to the GI because Q -values there fall below the threshold value of $\sqrt{3}$ (83).

We calculate the effective α_{GI} parameter, which is often invoked to measure the efficiency of mass transport by gravitational torques in protoplanetary disks (25), by

$$\alpha_{GI} = \frac{G_{r\phi}}{P \left| \frac{d \ln \Omega}{d \ln r} \right|},$$

where P is the gas pressure at the disk midplane and $G_{r\phi}$ is the (r, ϕ) component of the gravitational stress tensor in the disk plane (84),

$$G_{r\phi} = \frac{1}{4\pi Gr} \frac{\partial \Phi}{\partial r} \frac{\partial \Phi}{\partial \phi}$$

where Φ is the gravitational potential in the disk midplane. Using α_{GI} as a proxy for the efficiency of mass and angular momentum transport is justified for our disk because the disk-to-star mass ratio is sufficiently high, ≥ 0.2 (85) (see Fig. 4).

The magnetorotational instability (MRI) can drive turbulence that destroys dead zones and prevents planetesimal formation in magnetically active disks. Magnetic fields could be present in our disk, even in the absence of metals. Turbulent subgrid dynamos in principle can build up disordered magnetic fields that are later ordered and amplified by rotation in primordial disks (86-88). However, the degree to which those field lines would be coupled to gas in the disk and ramp up turbulence via the MRI is much less certain, for several reasons. Ohmic resistivity and ambipolar diffusion reduce the coupling of magnetic fields and gas and dampens the MRI (89). Thermal ionization fractions due to alkali elements would be 25 times lower than those in disks at solar metallicity because our disk is at $0.04 Z_{\odot}$, and smaller ionization fractions exacerbate Ohmic resistivity and ambipolar diffusion, further dampening the MRI. The odd-even effect in PI SNe, in which even-numbered elements are preferentially synthesized over odd-numbered elements during the explosion (5), suppresses the abundances of alkali elements in the disk by another two orders of magnitude, even further reducing thermal ionization fractions and weakening the MRI. Finally, there are few sources of non-thermal ionization such as cosmic rays because SNe were sparse in the primordial Universe. The PI SN remnant in which the disk formed likely produced cosmic rays but with fluxes that were certainly lower than those in the Galaxy today. These points are corroborated by recent work that found that the frequency of MRI bursts in magnetically layered disks is greatly reduced at low metallicities (90). Because our disk is not a strong candidate for the MRI we do not include it in our simulations.

Nevertheless, we ran a model that approximated the effect of the MRI by setting $\alpha = 10^{-2}$ where temperatures in the disk exceed 1000 K and thermal ionizations become important and $\alpha = 10^{-4}$ everywhere else. This is more stringent than in other planetesimal simulations that adopt anisotropic $\alpha = 10^{-3}$ in the plane of the disk and 10^{-4} in the vertical direction. In this simple but severe treatment, $0.7 M_{\oplus}$ of planetesimals still form in the disk, showing that the MRI suppresses but does not prevent rocky planet formation. Our approximation to the MRI also assumes solar metallicity by not taking into account the much lower potassium fractions discussed above and is truly a maximum upper limit to the impact of the MRI on planet formation here.

We show the evolution of the azimuthally averaged α_{GI} parameter as a function of radius and time in Fig. S4. The lowest α_{GI} are near the disk's inner edge and they systematically increase towards the disk's outer regions. This positive radial gradient in α_{GI} has a bottleneck effect: mass that is efficiently transported inward across the disk by gravitational torques accumulates in the innermost disk regions where transport by the GI is suppressed (91). A dead zone forms with characteristics similar to those in a layered disk model (92) because the GI is suppressed by high temperatures and strong shear. We note that α_{GI} is negligible prior to the formation of the disk ($t < 25$ kyr) and later beyond the disk because the spatial distribution of matter is nearly axisymmetric and gravitational torques are small. The α_{GI} profile in our disk is similar to those in other recent simulations (93), an independent confirmation of the physics in our model.

Fig. S5 shows the time evolution of other azimuthally averaged disk properties. Because of the bottleneck effect described above, gas accumulates at about 1.0 AU (panel a). A gas pressure maximum appears in this region (panel e), in which inward-drifting grown dust is decelerated and accumulated (94). Panels (d) and (f) indicate that dust grows above 1.0 mm and the Stokes number becomes greater than 10^{-2} , implying efficient inward radial drift. The accumulation of dust in the inner 1.0 AU triggers a positive feedback loop by raising the gas temperature because of the greater optical depth in this region, $\tau = \kappa \Sigma_{\text{d}}$, where κ is the dust opacity. Higher temperatures make the pressure peak even stronger.

Dust accumulation saturates when the streaming instability appears and grown dust begins to coagulate into planetesimals about 20 kyr after the formation of the disk. We show the dust surface density in the central 3.0 AU at 60 kyr as a space-time plot and a two-dimensional distribution in Fig. S7. The green contours highlight disk regions where the streaming instability operates according to the criteria laid out in Eqs. 2 and 3. This analysis confirms that planetesimals form interior to 1.0 AU and that planetesimal formation peaks between 20 and 40 kyr after the formation of the protostar (Fig. 4). Fig. S8 confirms that the streaming instability can develop in our model disk not only according to the criteria laid out in Equations 2 and 3, but also to criteria proposed in other studies (95).

Luminosity bursts brighter than a few tens of L_{\odot} (L_{\odot} , solar luminosity) appear in the disk 40 kyr after the formation of the protostar. These events, like those in the Milky Way (28), are due to episodic increases in accretion rate, \dot{M} , onto the protostar, but their origin is different. Outbursts in protostars today, known as FU~Orionis-type objects, are thought to be caused by the thermal, magnetorotational, or gravitational instability (60, 96, 97), by gravitational perturbations during close stellar encounters or infall of compact prestellar clouds (98, 99), or by planet-disk interactions (100). Here, the bursts are caused by short episodes of gravitational instability in the

innermost disk, as seen in the strong spiral-like gas density perturbation in panel (a) of Fig. S9. These episodes are accompanied by an increase in turbulent viscosity and local heating, as shown in panels (c) and (e). After a few orbital periods the perturbation is spread over the entire azimuth, warming up the innermost disk above 1000 K as seen in panel (d). As a result, \dot{M} rises sharply by factors 10-100.

The gravitational energy of this accreted matter is transformed into heat and radiated away as accretion luminosity, $L_{\text{acc}} = 0.5 GM_* \dot{M} / R_*$, where M_* and R_* are the mass and radius of the protostar. The accretion luminosity during the bursts greatly exceeds that of the photosphere, which is powered by deuterium burning and compressional heating. As shown in Fig. S10, luminosity bursts regulate the conversion of dust to planetesimals by evaporating some of the dust by heating the inner disk. The sublimated dust mass exceeds that of the dust remaining in the disk after ~ 50 kyr. Some of the dust vapor is accreted onto the protostar with the gas but some may return as sub- μm dust seeds as the disk cools after the burst, but they are not included in our simulation.

The streaming instability converts dust to planetesimals, which then grow into solid planets either via oligarchic collisional growth (33) or pebble accretion (35). We can estimate the mass reservoir of pebbles in the disk by applying the following definition of pebbles (101). First, we assume that pebbles are dust particles with sizes $a_{\text{peb},0} \geq 0.5$ mm. This lower limit is motivated by the typical sizes of chondrules, 0.1 - 1.0 mm (102). Second, we stipulate that pebbles are larger than dust grains with size $a_{\text{St}0}$ that have $St_0 = 0.01$ locally in the disk, meaning that they can decouple dynamically from gas and can be accreted by a protoplanetary core. These two conditions define the minimum size of pebbles as

$$a_{\text{peb},\text{min}} = \begin{cases} a_{\text{St}0}, & \text{if } a_{\text{St}0} > a_{\text{peb},0}, \\ a_{\text{peb}}, & \text{if } a_{\text{St}0} \leq a_{\text{peb},0}. \end{cases}$$

Previous studies have examined the effects of variations in $St_0 = 0.01$ and $a_{\text{peb},0} = 0.5$ mm (101). As shown in Fig S6, the protoplanetary disk has on average several M_{\oplus} of pebbles, which increases the likelihood of terrestrial-type planet formation in the debris of the PI SN explosion.

To explore the limits within which our conclusions remain valid, we considered variations in the fragmentation velocity, v_{frag} , and the dust-to-gas mass ratio of the PI SN core, $\xi_{\text{d}2\text{g}}^{\text{init}}$. We also considered more recent streaming instability criteria (95). Fig. S11 shows the mass of planetesimals formed in these models as a function of time. Lowering the value of $\xi_{\text{d}2\text{g}}$ has the strongest effect, reducing the mass of planetesimals to much below that of Earth. The other models yield total planetesimal masses that vary by a factor of a few but are still above $1 M_{\oplus}$.

We can estimate the radii at which liquid water can exist in the planetary system that will later evolve from the disk after it has been dispersed (103, 104) with a method that is valid for stars with masses and metallicities similar to the one in our model (105). The time evolution of the water line can be described as

$$d_{\text{HZ}}(t) = \frac{1}{a} \sqrt{\frac{(1-A)L(t)}{16\pi\sigma}} \frac{1}{T_{\text{p}}^2},$$

where σ is the Stefan-Boltzmann constant and $L(t)$ is the luminosity of a star with age t , mass M_* , metallicity Z , and helium-to-metal enrichment ratio $\Delta Y/\Delta Z$. We set $M_* = 0.7 M_\odot$, assuming a 70% cloud-to-star conversion efficiency (106), and $Z = 0.005$, which is the closest value available to our models. The albedo A is set equal to the Earth's average Bond value $A = 0.3$ (107) and $\Delta Y/\Delta Z = 0.2$. The planet's equilibrium temperature T_p , the temperature at which the absorbed and radiated fluxes are at equilibrium, is set to 269 K at the innermost water line (108). We set $T_p = 186$ K at the outermost line, which is the arithmetic average of the temperatures derived from atmospheric models with CO₂ and H₂O greenhouse effects, $T_p = 169$ K, and those that also include CO₂ ice clouds, $T_p = 203$ K (103, 105). The coefficient a is the conversion factor from cm to AU. The two boundaries for water that remains in liquid form for more than 4.0 Gyr are shown in Fig. 3. We checked if this method agrees with the bounds reported for the Sun, which yields 0.88 AU for the inner boundary and 1.81 AU and 2.64 AU for the outer boundary for the respective equilibrium temperatures of 169 K and 203 K. These bounds agree within a factor of unity with those in the literature (109, 110).

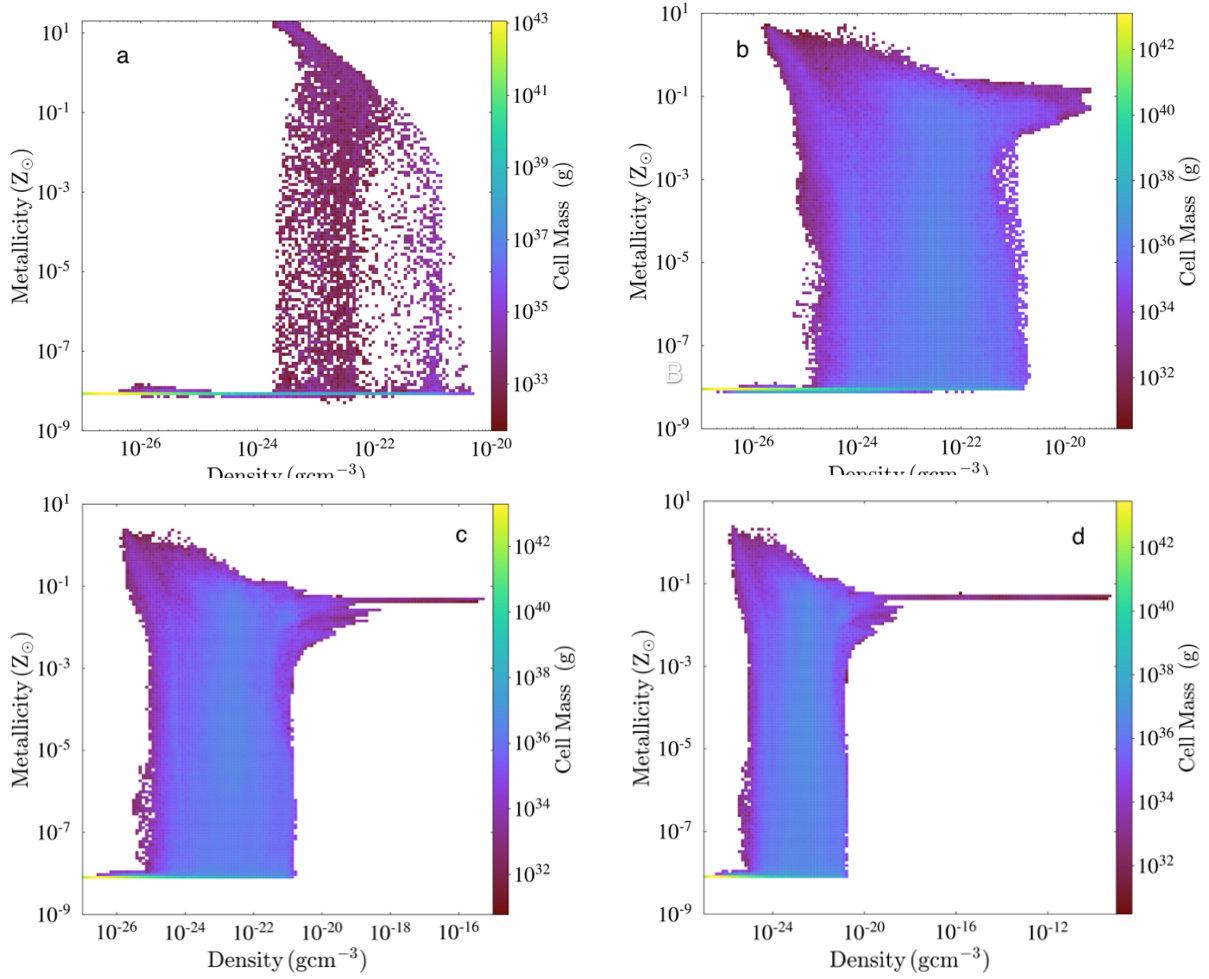


Fig. S1. **Formation of the dense core.** The initial rapid enrichment of gas in the PI SN bubble is shown at 0.333 Myr after the explosion in the phase diagram in (a), in which the dense shell ($\sim 100 \text{ cm}^{-3}$) swept up by the ejecta has already reached metallicities $Z \sim 10^{-2} - 10^{-3} Z_{\odot}$. The appearance of a turbulent density fluctuation with $n \sim 10 \text{ cm}^{-3}$ and $Z \sim 0.1 - 0.01 Z_{\odot}$ at 1.86 Myr can be seen in (b). The emergence of the dense core in $Z = 0.04 Z_{\odot}$ gas at 3.05 Myr is shown in (c), and the runaway collapse of the core at 3.063 Myr is clearly visible in (d).

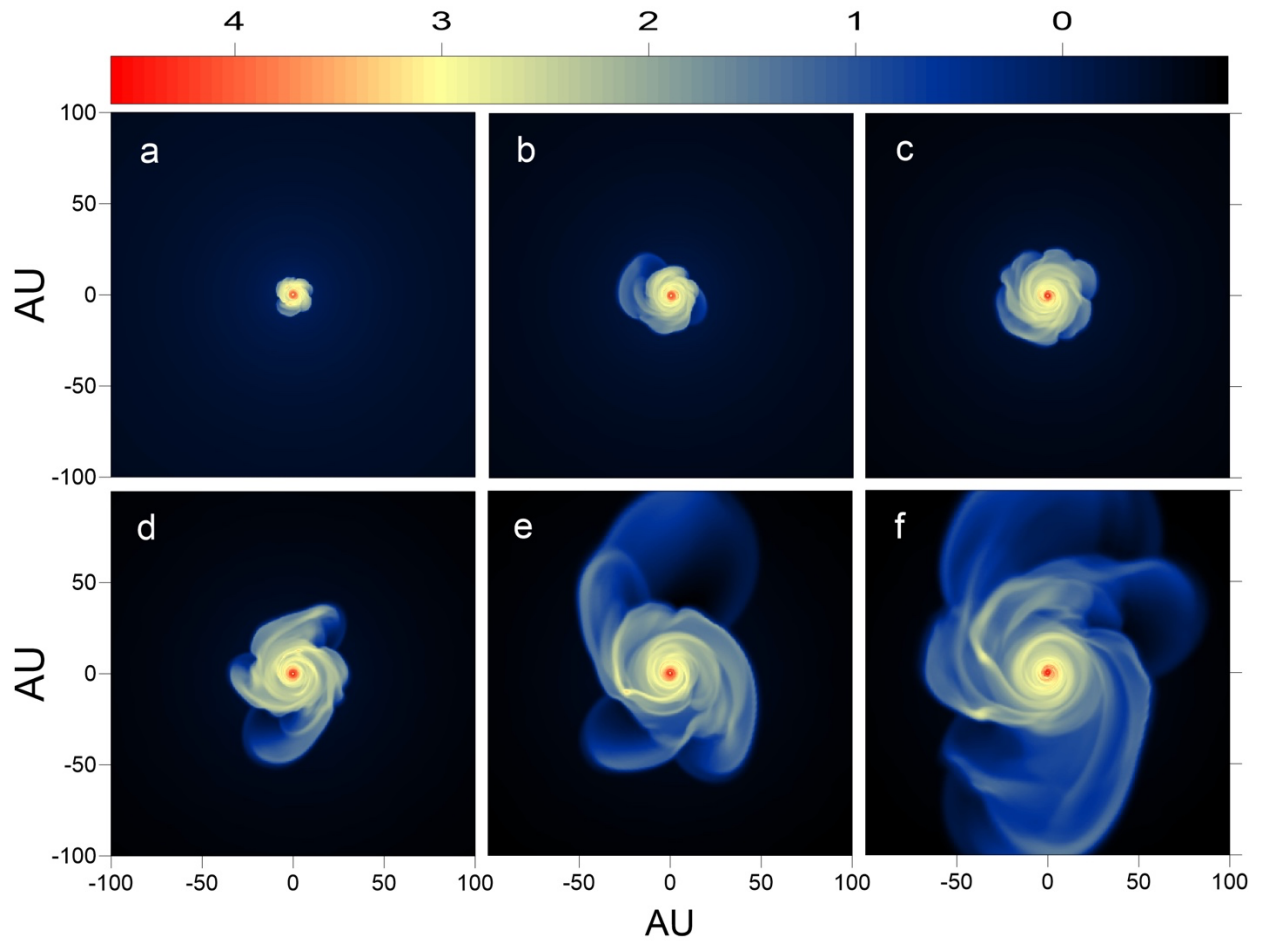


Fig. S2. Formation and growth of the disk. Gas surface densities (in g cm^{-2}) for the inner 200 AU of the disk are shown at 13, 21, 30, 40, 50 and 60 kyr in (a) – (f).

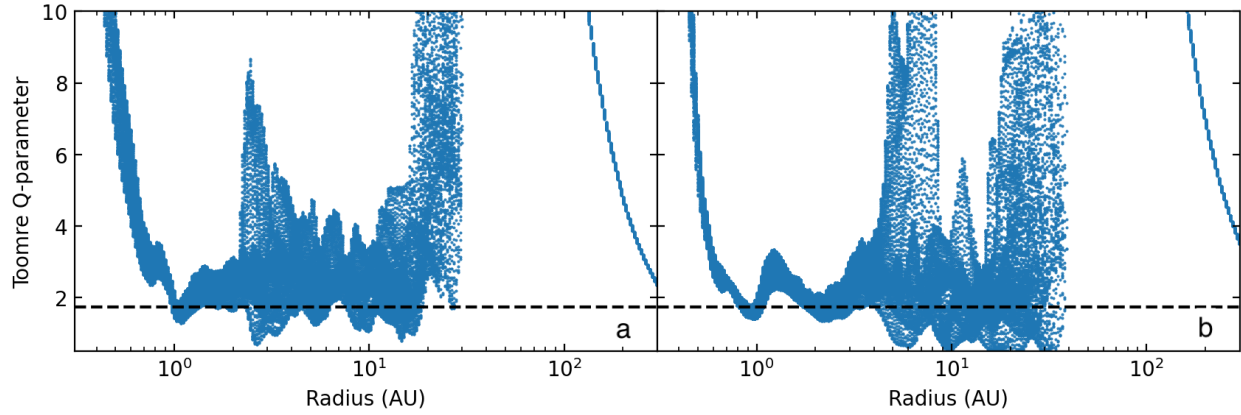


Fig. S3. **Stability of the disk.** Radial profiles of the Toomre Q -parameter are shown at 30 and 40 kyr in (a) and (b). The horizontal dashed line marks the threshold value of below which the gravitational instability develops.

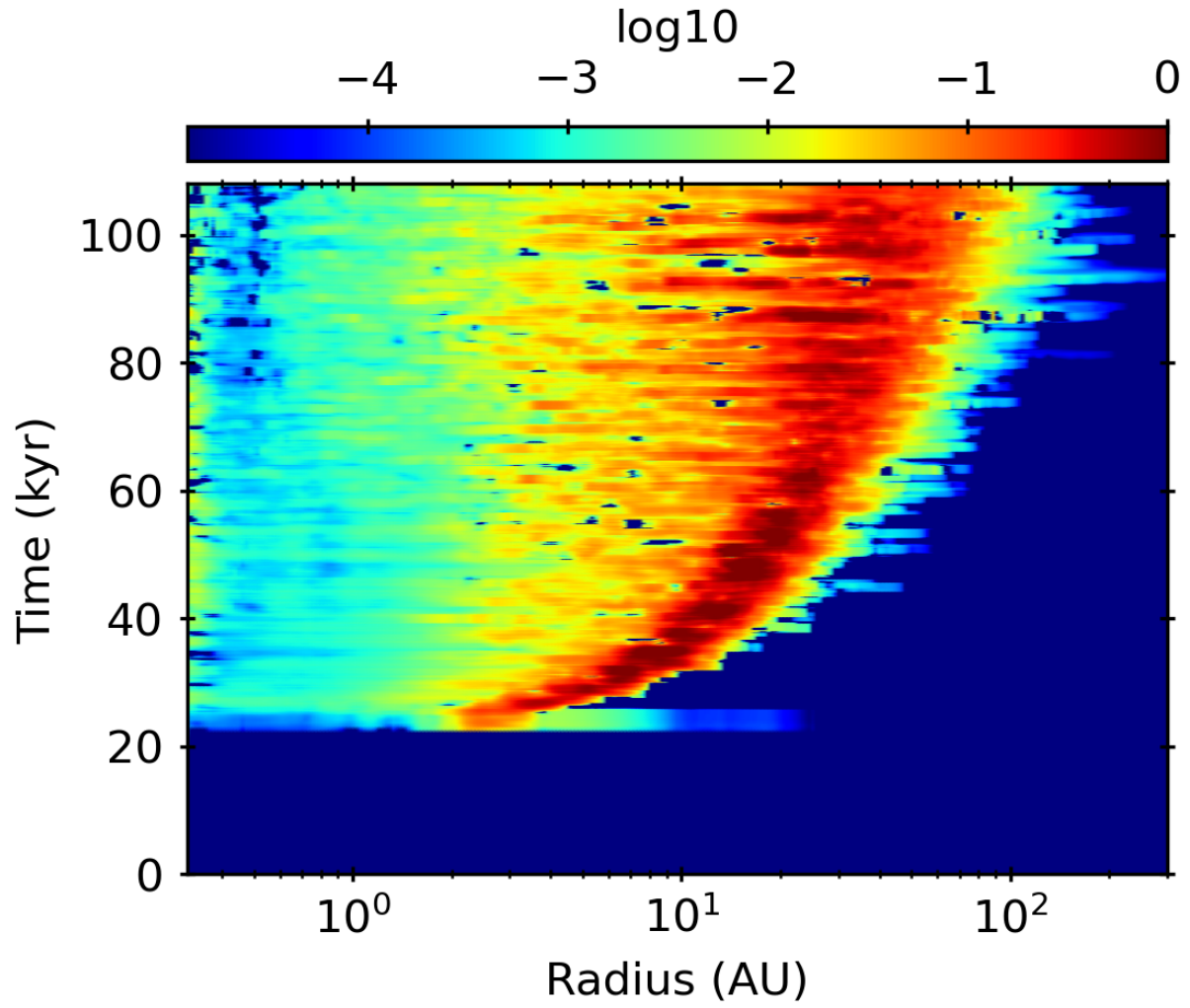


Fig. S4. **Effective α_{GI} parameters for the disk.** The radial gradient in α after disk formation at $t \sim 25$ kyr is positive.

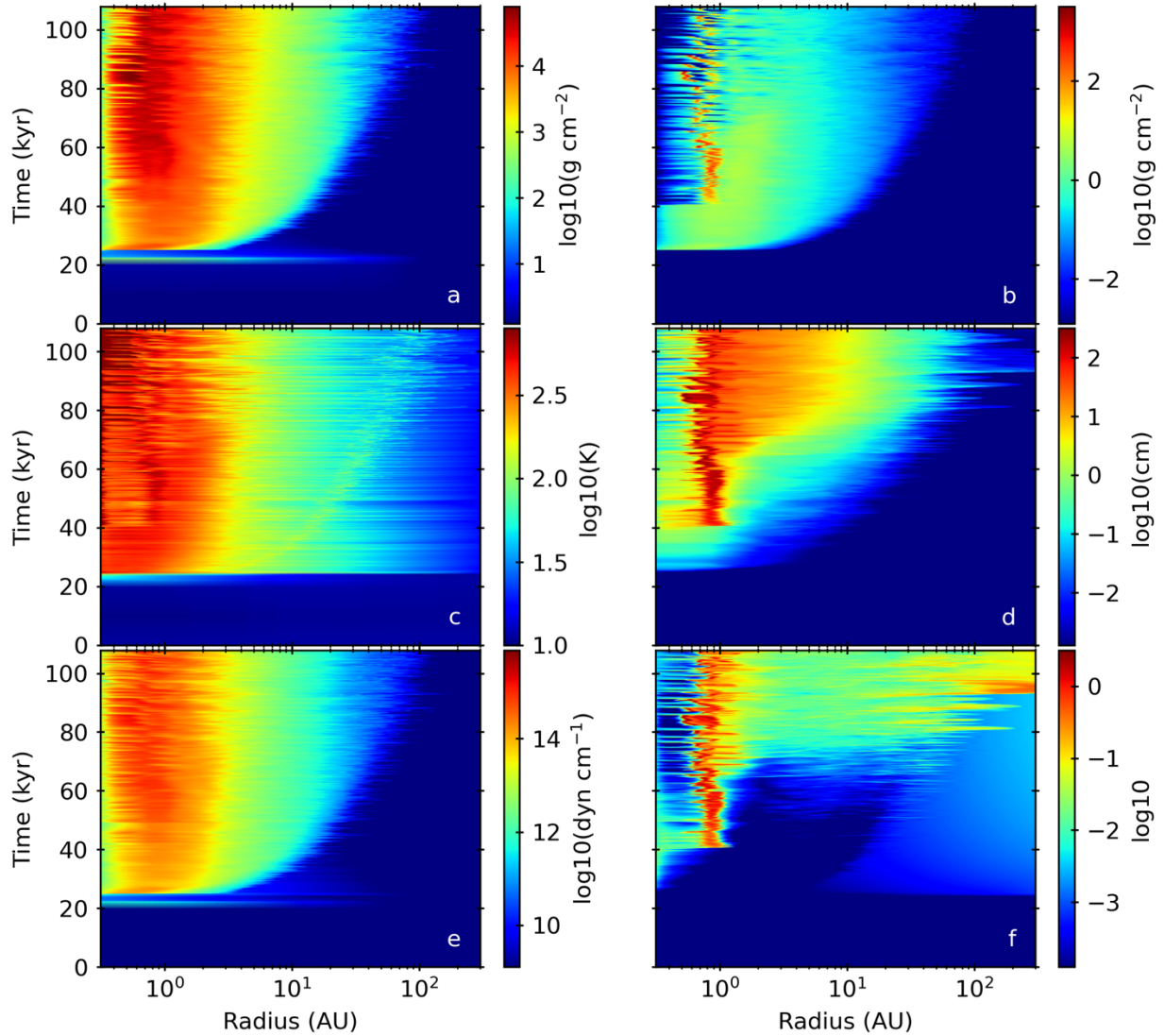


Fig. S5. Evolution of disk properties over time. Azimuthally averaged gas surface densities, dust surface densities, gas temperatures, maximum dust grain sizes, vertically integrated gas pressures, and Stokes numbers for the disk are shown in (a) – (f), respectively.

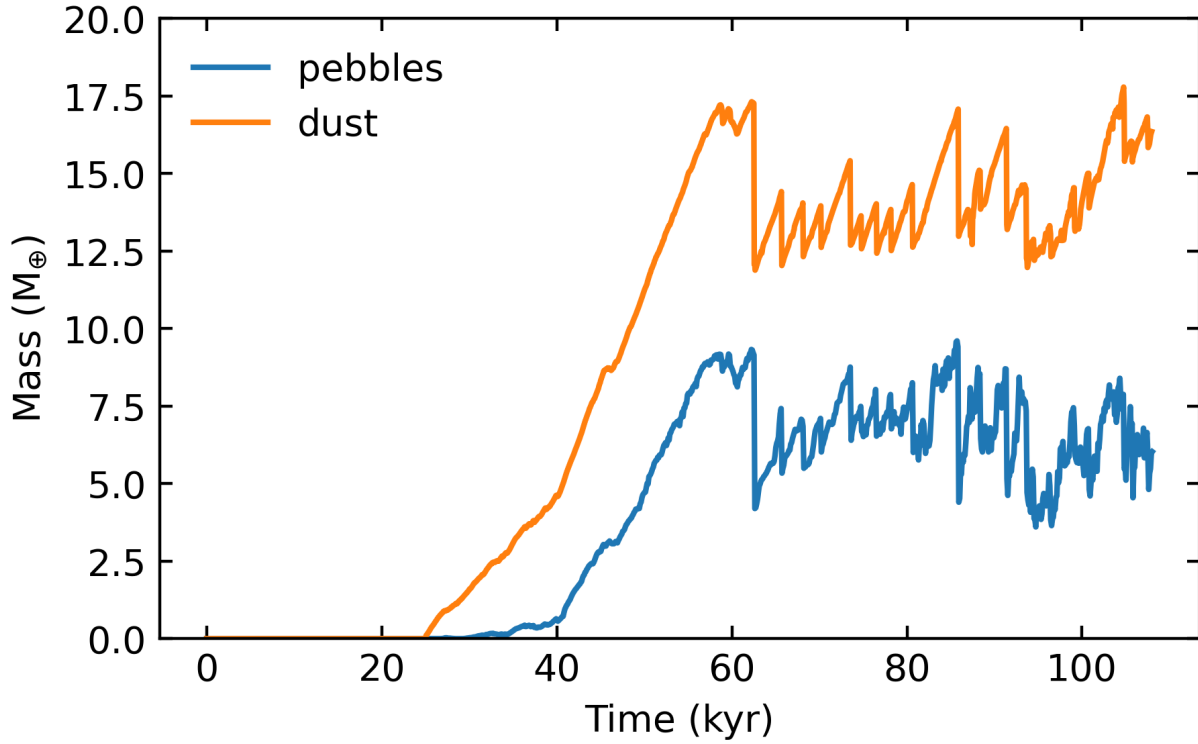


Fig. S6. Dust and pebble masses in the disk.

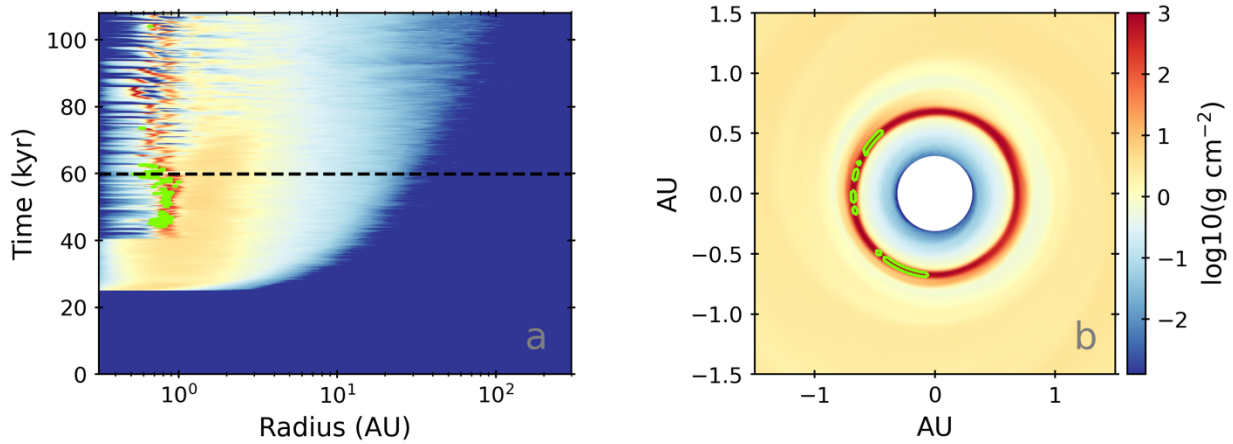


Fig. S7. **Dust surface densities.** Dust surface densities are shown as a function of time in (a) and as a two-dimensional snapshot 60 kyr after the onset of clump collapse in (b). The green contours outline the disk regions where the streaming instability develops. The dashed horizontal line in (a) marks the time at which the 2D spatial distribution of dust is shown in (b).

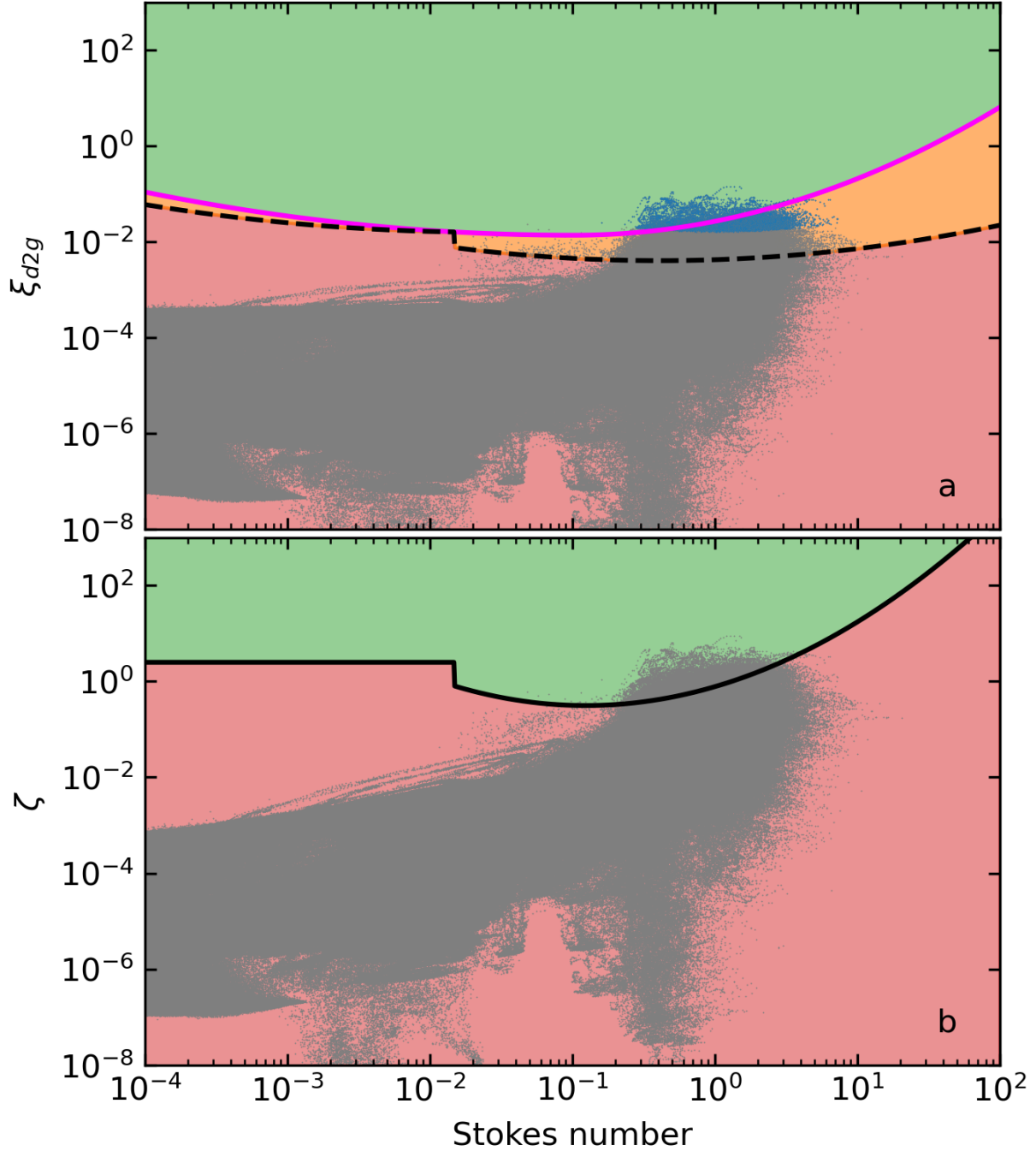


Fig. S8. **Streaming instability phase space.** Panel (a) shows the ratio of the surface densities of grown dust to gas, ξ_{d2g} , as a function of the Stokes number. The pink and dashed black lines mark the critical values for the development of the streaming instability (79, 95). Panel (b) shows the ratio of the volume densities of grown dust to gas, ζ , as a function of Stokes number. The solid black line indicates the critical values for the streaming instability (95). The data of our model are overlaid with filled circles, with blue ones fulfilling in addition the criterion on the ratio of volume densities.

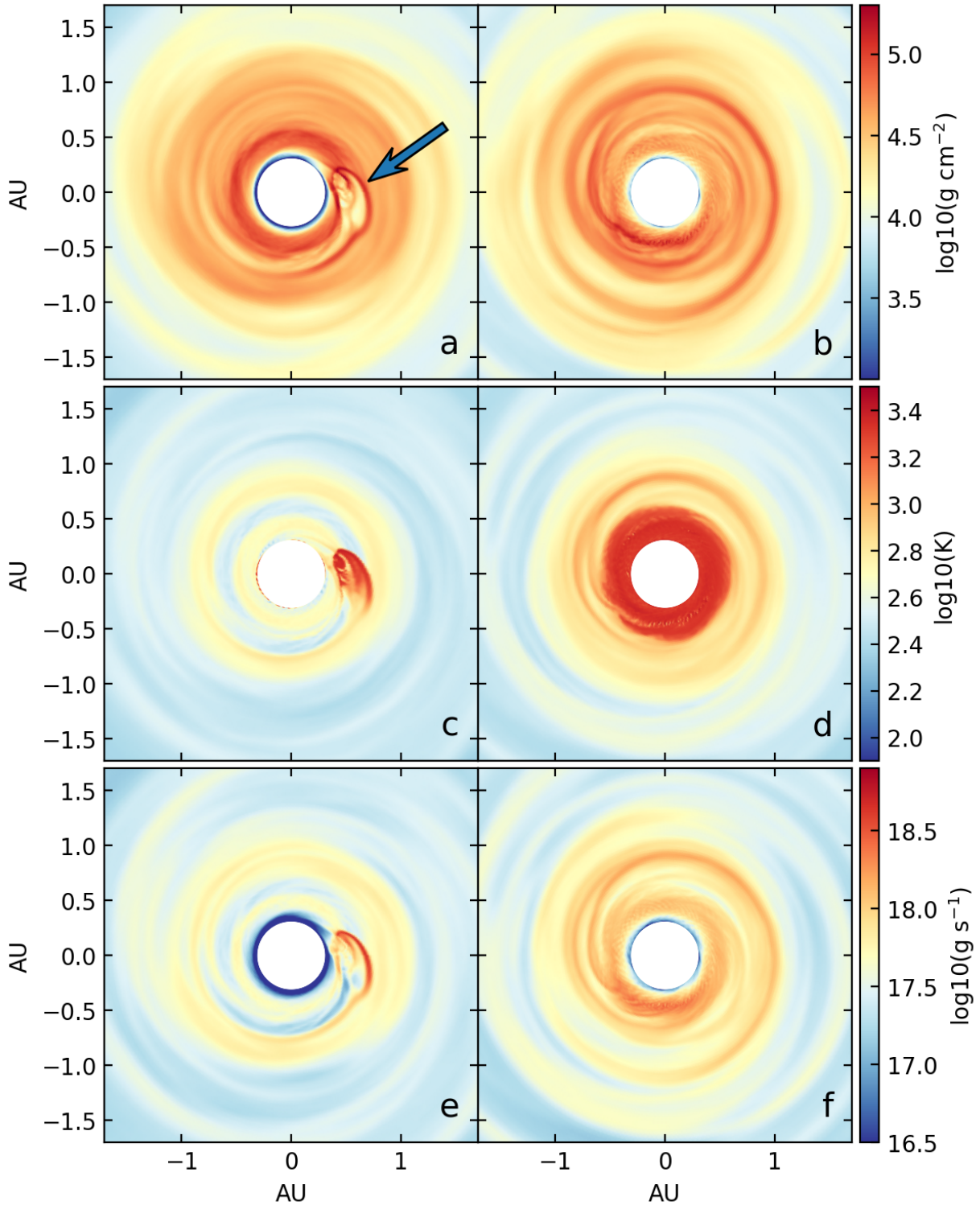


Fig. S9. **The origin of accretion bursts.** The central 3 AU of the disk just before (a, c and e) and during (b, d, and f) a protostellar accretion burst. Rows from top to bottom show gas surface densities, gas temperatures, and turbulent dynamical viscosities. The arrow indicates a local density disturbance that produces viscous heating in the inner disk.

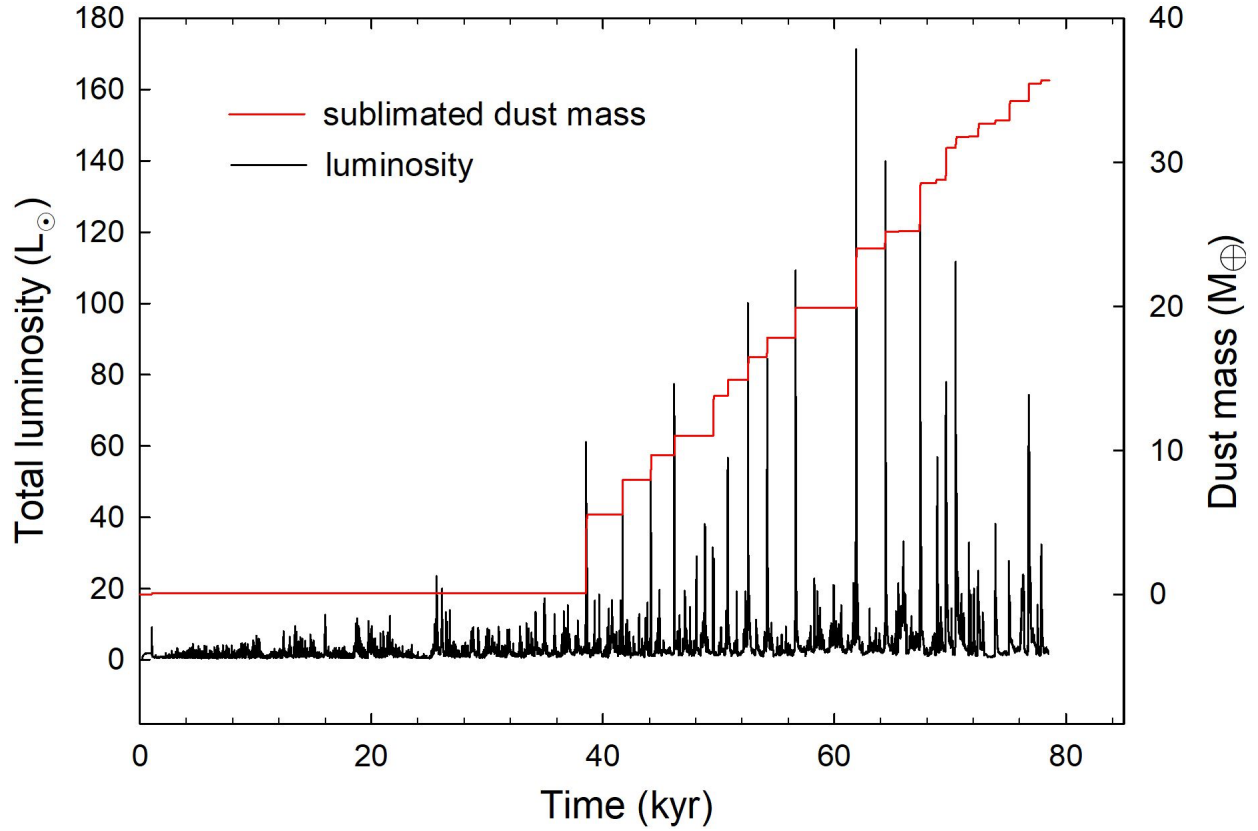


Fig. S10. **Luminosities and dust sublimation in the disk.** Total luminosities (accretion plus photospheric) and evaporated dust masses as a function of time from the onset of clump collapse.

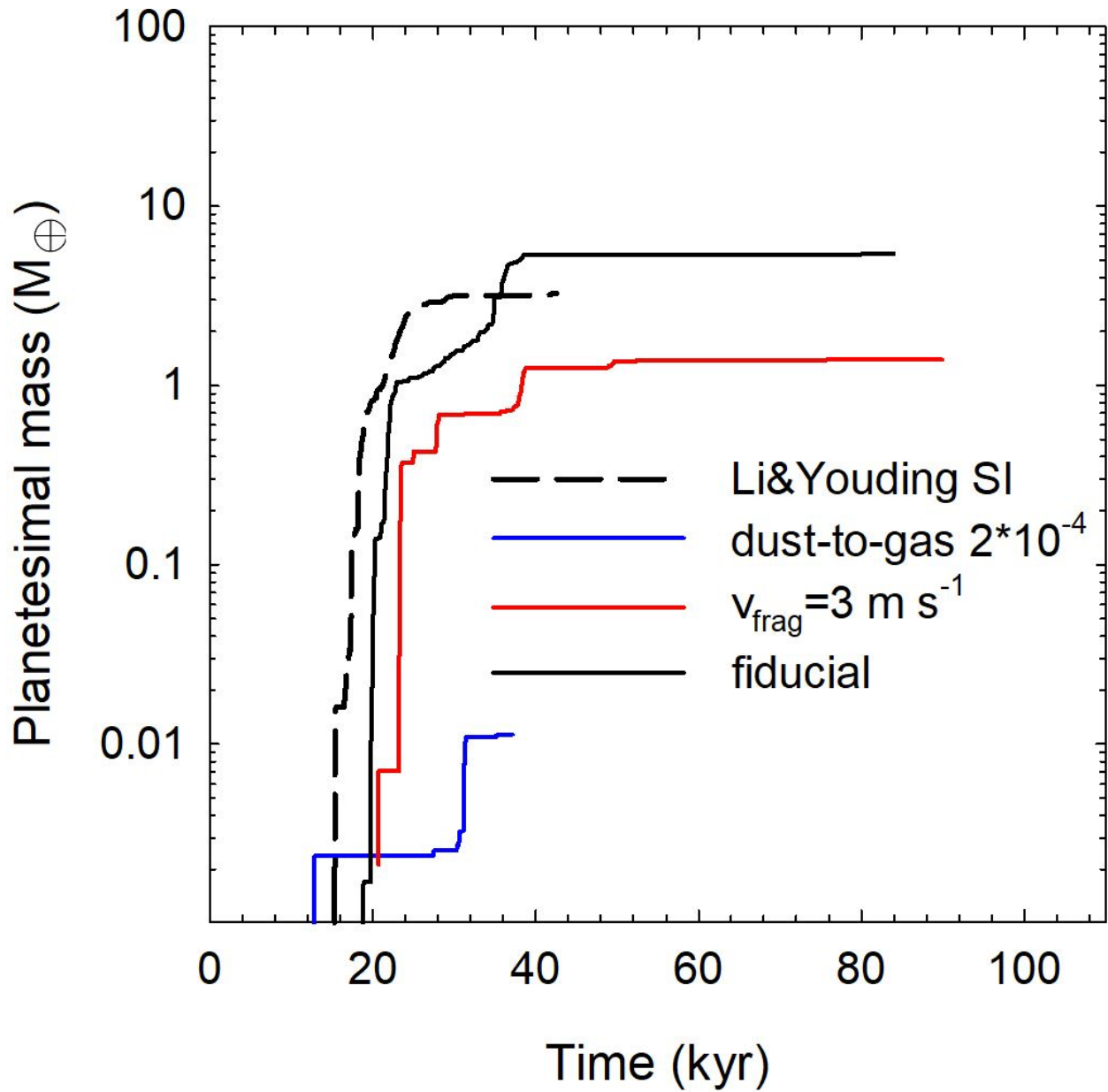


Fig. S11. **Total planetesimal mass as a function of time.** The curves are the fiducial model (solid black), the model with the fragmentation velocity set equal to 3.0 m s^{-1} (solid red), the model with $\xi_{\text{d2g}}^{\text{init}} = 2 \times 10^{-4}$ (solid blue), and the model with the streaming instability criteria taken from Li & Youdin (2021) (104) (dashed black).